



Mesgarpour, M., Abad, J. M. N., Alizadeh, R., Wongwises, S., Doranehgard, M. H., Ghaderi, S. and Karimi, N. (2021) Prediction of the spread of Corona-virus carrying droplets in a bus- a computational based artificial intelligence approach. *Journal of Hazardous Materials*, 413, 125358. (doi: [10.1016/j.jhazmat.2021.125358](https://doi.org/10.1016/j.jhazmat.2021.125358)).

This is the author's final accepted version.

There may be differences between this version and the published version. You are advised to consult the publisher's version if you wish to cite from it.

<http://eprints.gla.ac.uk/233460/>

Deposited on: 05 February 2021

Enlighten – Research publications by members of the University of Glasgow  
<http://eprints.gla.ac.uk>

# Prediction of the spread of Corona-virus carrying droplets in a bus- A computational based artificial intelligence approach

Mehrdad Mesgarpour<sup>1</sup>, Javad Mohebbi Najm Abad<sup>2</sup>, Rasool Alizadeh<sup>3</sup>, Somchai Wongwises<sup>1,4</sup>, Mohammad Hossein Doranehgard<sup>5</sup>, Saeidreza Ghaderi<sup>6</sup>, Nader Karimi<sup>7,8</sup>

<sup>1</sup>Fluid Mechanics, Thermal Engineering and Multiphase Flow Research Lab. (FUTURE), Department of Mechanical Engineering, Faculty of Engineering, King Mongkut's University of Technology Thonburi (KMUTT), Bangmod, Bangkok 10140, Thailand

<sup>2</sup>Department of Computer Engineering, Quchan Branch, Islamic Azad University, Quchan, Iran

<sup>3</sup>Department of Mechanical Engineering, Quchan Branch, Islamic Azad University, Quchan, Iran

<sup>4</sup>National Science and Technology Development Agency (NSTDA), Pathum Thani 12120, Thailand

<sup>5</sup>Department of Civil and Environmental Engineering, School of Mining and Petroleum Engineering, University of Alberta, Edmonton, Alberta, T6G 1H9, Canada

<sup>6</sup>Department of General Surgery, Shahid Modarres Hospital, Shahid Beheshti University of Medical Sciences, Tehran, Iran

<sup>7</sup>School of Engineering and Materials Science, Queen Mary University of London, London E1 4NS, United Kingdom

<sup>8</sup>James Watt School of Engineering, University of Glasgow, Glasgow G12 8QQ, United Kingdom

## Abstract:

Public transport has been identified as high risk as the corona-virus carrying droplets generated by the infected passengers could be distributed to other passengers. Therefore, predicting the patterns of droplet spreading in public transport environment is of primary importance. This paper puts forward a novel computational and artificial intelligence (AI) framework for fast prediction of the spread of droplets produced by a sneezing passenger in a bus. The formation of droplets of saliva is numerically modelled using a volume of fluid methodology applied to the mouth and lips of an infected person during the sneezing process. This is followed by a large eddy simulation of the resultant two phase flow in the vicinity of the person while the effects of droplet evaporation and ventilation in the bus are considered. The results are subsequently fed to an AI tool that employs deep learning to predict the distribution of droplets in the entire volume of the bus. This combined framework is two orders of magnitude faster than the pure computational approach. It is shown that the droplets with diameters less than 250 micrometers are most responsible for the transmission of the virus, as they can travel the entire length of the bus.

**Keyword:** COVID-19; Droplet distribution; Large Eddy Simulations; Deep Neural Network; Prediction.

## Graphical abstract:

<i>Nomenclature</i>			
$AI$	Artificial intelligence	$\Delta T^m$	Mixture temperature gradient
$C_{1M}^{2\sigma}$	Vapor mass concentration of the surface	$T_3^{1\sigma}$	Vapor temperature (partial surface)
$C_{1M}$	Mass concentration of a gaseous component	$u^{m*}, v^{m*}, w^m$	Velocity component for n <sup>th</sup> fluid

$C_D$	Drag coefficient of droplets	$V$	Airflow velocity
$C_{M1}^{3\sigma}$	Partial surface concentration of the vapor	$t$	Time
$c_3$	Constant parameter	$U^{dr,m^*}$	Drift velocity vector of the k <sup>th</sup> phase
$D$	Hydraulic particle diameter	$U_{wall}$	Wall velocity
$D_3$	Constant parameter	$u_t$	Tangential velocity component
$D_{M \rightarrow \Sigma n}$	Hydraulic diameter for droplet	$U^m$	Mixture velocity
$d_p$	Diameter of the droplet	$V_{ins}^f$	Volume of fluid (initial state)
$F_{Body}$	Body force	$V_{ins}^p$	Volume of the second phase (initial state)
$F_{Drag}$	Drag force	$V_a$	Air velocity
$F_{Added}$	External force	$V_p$	Volume of the second phase
$g$	Gravity	$x - y - z$	Coordinates, m
$H^{m^*}$	Enthalpy for n <sup>th</sup> fluid	<b>Greek symbol</b>	
$H^m$	Enthalpy by the combination of phase-weighted	$\Theta$	Stress field for the two phase flow
$h_{M1}^{3\sigma}$	Specific enthalpy for liquid (phase 1)	$\beta$	Slip coefficient
$h_{M3}^{3\sigma}$	Specific enthalpy for vapor (phase 3)	$\alpha^m$	Volume fraction of the mixture
$h_{fg}$	Heat transfer coefficient between fluid and gas	$\alpha^{m^*}$	Volume fraction for N <sup>th</sup> fluid phase
$h$	Specific enthalpy	$\mu_T^{m^*}$	Turbulent viscosity of the continuous n <sup>th</sup> phase
$J_w$	Evaporation of droplet	$\rho^{m^*}$	Density for n <sup>th</sup> fluid
$k$	Turbulence kinetic energy	$\mu^{m^*}$	Viscosity for n <sup>th</sup> fluid
$m^*$	m <sup>th</sup> fluid phase	$\alpha_3$	Constant parameter
$p_{M1}^{3\sigma}$	Partial surface pressure of the vapor	$\varepsilon$	Turbulence dissipation
$P_w$	Partial saturated vapor pressure	$\mu_m$	Mixture viscosity
$P_{V,i,U}$	Ratio of the volume of all the particles with diameters in size class I	$\zeta$	Relaxation factor (functional)
$p$	Pressure	$\Gamma^{m^*}$	Favre-averaged quantity
$P_a$	Partial water vapor pressure	$\lambda^{m^*}$	Thermal conductivity for n <sup>th</sup> fluid phase
$q_H^{m^*}$	Heat flux for n <sup>th</sup> fluid (droplet enthalpy)	$\sigma$	Capillary force
$q^{m^*}$	Heat flux for n <sup>th</sup> fluid	$\tau$	Response time
$RH$	Relative humidity	$\rho^f$	Fluid density
$Re$	Reynolds number	$\rho^m$	Mixture density
$S_{m^{m^*}}^{int}$	The interface between phases for mass	$\lambda^m$	Mixture thermal conductivity

$S_{u^{m^*}}, S_{v^{m^*}}, S_{w^{m^*}}$	Source or sink terms	$\rho$	Density
$S$	Rate of strain tensor for the resolved scale	$\rho_l$	Density of the liquid phase
$T_{ambient}$	Temperature		

34

### 35 **1. Introduction**

36 The spread of Corona-virus via droplets generated by human sneezing and coughing has attracted a significant attention  
37 in recent months. It has been shown that this process can enhance the virus transmission by 18 times [1-4]. Dispersion  
38 of the droplets produced by human sneezing is a complex physical process [5, 6]. Upon leaving the mouth, the saliva  
39 droplet is broken down into smaller droplets. The subsequent evaporation of droplets and reduction of diameters cause  
40 drastic changes in their deposition and suspension. This highly complicates the development of predictive models for  
41 spread of such droplets and the subsequent transmission of the virus [7,8].

42 A considerable amount of work has been already done on modelling of sneezing. In 2019, Hassani and  
43 Khorramymehr [9] studied the process of transmitting sneezing generated droplets into human airways. The results  
44 showed that for an average flow rate of 4.79 L/s, the airflow outlet velocity from the mouth reaches 5.3 and 8.4 m/s,  
45 respectively. In 2020, Singh and Tripathi [10] numerically simulated the dispersion of sneezing particles in a room.  
46 Their investigation was complimented by an experiment and put forward a model for measuring the transfer of particles  
47 in surrounding air. This was continued by Kotb and Khalil [11] with a numerical study of the emission of particles  
48 containing SARS-COVID 19 virus into the interior of a passenger aircraft. The result indicated that velocity of the  
49 droplets produced by the moving passengers could reach the seated passengers. However, sneezing generated droplets  
50 had more harmful impacts than those produced by coughing, while both traveled a long distance inside the cabin.

51 Most recently, Busco et al. [12] conducted a comprehensive study of the spread of the virus in the environment  
52 and showed that the deposition of different particles is a function of their average diameter. They further argued that  
53 environmental effects play a major role in particle dispersion. In another study, Li and et al. [13] investigated the  
54 emission model of sneezing droplets and concentration of the resultant particles in the environment. Through an  
55 analysis of the effects of ventilation on the spread of the virus in a room, Ali Hasan [14] showed that the intensity and  
56 direction of airflow inside the room significantly affect the dispersion model. Chaudhuri et al. [7] developed a model of  
57 droplet distribution based on reaction. Their model was validated against the experimentally obtained evaporation data  
58 of levitated droplets of pure water and salt solution. As expected, the droplet evaporation time was found to be  
59 dependent on the ambient temperature and was also a strong function of relative humidity. Verma et al. [15] showed  
60 that the use of protective shields can have a significant effect on the pattern of droplets diffusion as well as the spread  
61 of contamination in the sneezing process. Abuhegazy et al. [8] examined the emission model of aerosols in air, and found  
62 that these particles could be easily transported in the environment by the ambient flow.

63 In general, numerical methods provide a convenient framework to study dispersion of the virus carrying droplets.  
64 Hence, a number of researchers tried to detect virus transmission routes via numerical simulations [1-8]. Table 1

65 presents an outline of the latest research articles on the applications of computational particle science combined with  
 66 computational fluid dynamics.

67 Table 1. List of the most recent investigations that employed a combination of CFD and particle science.

No.	Model	Dimensions	Particle/ Droplet size (mm)	Domain	Turbulence method	Target	Solver	Ref.
1.	Unsteady-DPM	2D	0.1-0.3	tube banks	k- $\omega$ (SST)	Deposition particle	Ansys Fluent	[16]
2.	Unsteady-DPM	2D	0.012	cryogenic condenser	k- $\omega$ (SST)	Deposition particle	Ansys Fluent	[17]
3.	Unsteady- Lagrangian particle tracking	2D	0.001-0.01	airway	RANS	Particle flows	Ansys Fluent	[18]
4.	Unsteady-DPM	2D	0.001-0.05	ribbed duct air flows	RANS	Particle deposition	Ansys Fluent	[19]
5.	Unsteady-DPM	3D	0.001- 11.25	90-degree bend of natural gas pipelines	k- $\omega$ (SST)	Particle deposition	Ansys Fluent	[20]
6.	Lagrangian Particle Track	2D	0.002- 0.058	cyclone separator	RANS	Particle deposition	Ansys Fluent	[21]
7.	Unsteady-DPM	3D	0.002- 0.005	Nose-to-Lung	k- $\omega$ (SST)	Aerosol Delivery	Ansys Fluent	[22]
8.	Unsteady	3D	-	environment	LES	Breathing Simulations	Ansys Fluent	[23]
9.	Unsteady-DPM	2D	0.001- 0.009	lung	LES	Aerosol deposition	Ansys Fluent	[24]
10.	Unsteady-DEM	3D	0-0.002	inhalation indoors	Monte- Carlo	SARS-CoV-2 transmission		[25]
11.	Lagrangian method	2D	-	combustion	RANS	Ash deposition	In- house code	[26]

68

69 Public transport contributes significantly to transmission of COVID-19 [8]. As a result, there is a substantial  
 70 emphasis on the mitigation of transmission risk in public transport including buses and train carriages. This, in turn,

71 calls for prediction of the spread of the virus in indoor environments. In general, such predictions can be made by the  
72 conventional computational analyses. However, the associated computational burden forbids their use in practical risk  
73 assessments. As a remedy, the techniques from machine learning can be utilized to reduce the computational load. This  
74 will lead to the development of a data-driven model that uses the computationally generated data for a small section of  
75 the domain and extrapolates those. The effectiveness of such combined approach has been already demonstrated in the  
76 context of propulsion and process engineering [27-30]. It was shown that data-driven approaches could predict  
77 complicated spatiotemporal behaviors, while high fidelity computation was performed only for a small fraction of the  
78 domain [27]. Hence, the current study includes a computational part followed by artificial intelligence (AI). In the  
79 numerical study, computational fluid dynamics is used to model a three-phase flow of liquid droplets and water vapor  
80 in air during the droplet distribution process. This model is based on the changes in the particle diameters encountered  
81 in sneezing process and their transmission by air flow. Due to the large gradient in the sneezing process and the changes  
82 in the flow Reynolds number, an innovative model is developed for low cost and yet accurate analysis of high and low-  
83 speed flows. The numerical results are then fed into an AI-based soft tool, which predicts the droplet distribution inside  
84 a bus. This results in a novel combination of computational fluid dynamics and artificial intelligence, which forms an  
85 efficient tool for practical risk assessments.

## 86 **2. Problem Definition**

87 Buses are the most common means of public transport throughout the world and have specific features that make them  
88 pertinent to transmission of the virus. These include the high surface density of passengers and the lack of strong  
89 ventilation. In this study, one of the common types of urban buses is considered. Figure 1 shows a schematic view of the  
90 investigated (90 m<sup>3</sup> net capacity) bus along with its interior layout. By considering the seats and other components, the  
91 internal volume of the bus is about 80 m<sup>3</sup>. Here, it is assumed that the exit doors are closed. It should be noted that  
92 motion of the buses in urban areas is usually slow and does not involve significant accelerations. Thus, any effect made  
93 by the motion of the bus has been ignored.

94 Figure 1b shows the locations of the seats. In this configuration, 35 seats with the height of 1.20-meter were  
95 considered. Each seat has a 0.5-meter distance from the next one in front and a 10 cm gap on the side. To simplify the  
96 simulations, only one infected passenger was considered. As shown in Fig.1a, a standing passenger (1.80 meters of  
97 height) at the end of the bus is sneezing. The passenger is located on the center-plane of the bus. Steady-state airflow  
98 ( $V=0.1\text{m/s}$ ) is injected at the end of the bus. This system is closed and stays at constant temperature and humidity  
99 ( $T_{\text{ambient}}=20^{\circ}\text{C}$ ,  $\text{RH}=20\%$ ). All the walls and doors of the bus are assumed to be adiabatic. In the proceeding analysis, all  
100 fluids are assumed to be isotropic and Newtonian and, the flow is incompressible.

## 101 **3. Governing Equation**

102 The multiphase flow in this study contains liquid, gas and vapor phases. To model this complex, three phase flow, the  
103 conservation of mass and momentum in the Eulerian framework for any  $m^*$  fluid is written as [31-33]:

104 Conservation of mass:

$$\frac{\partial(\alpha^{m*} \rho^{m*})}{\partial t} + \frac{\partial(\alpha^{m*} \rho^{m*} u^{m*})}{\partial x} + \frac{\partial(\alpha^{m*} \rho^{m*} v^{m*})}{\partial y} + \frac{\partial(\alpha^{m*} \rho^{m*} w^{m*})}{\partial z} = S_{m^{m*}}^{\text{int}} \quad (1)$$

105 In this equation,  $t$ , is time and  $x,y,z$  are the three spatial coordinates.

106 Transport of momentum in  $x,y,z$  directions:

$$\begin{aligned} & \frac{\partial(\alpha^{m*} \rho^{m*} u^{m*})}{\partial t} + \frac{\partial(\alpha^{m*} \rho^{m*} u^{m*} u^{m*})}{\partial x} + \frac{\partial(\alpha^{m*} \rho^{m*} v^{m*} u^{m*})}{\partial y} + \frac{\partial(\alpha^{m*} \rho^{m*} w^{m*} u^{m*})}{\partial z} \\ &= \frac{\partial}{\partial x} \left[ \alpha^{m*} (\mu^{m*} + \mu_T^{m*}) \frac{\partial u^{m*}}{\partial x} \right] + \frac{\partial}{\partial y} \left[ \alpha^{m*} (\mu^{m*} + \mu_T^{m*}) \frac{\partial u^{m*}}{\partial y} \right] + \frac{\partial}{\partial z} \left[ \alpha^{m*} (\mu^{m*} + \mu_T^{m*}) \frac{\partial u^{m*}}{\partial z} \right] + S_{u^{m*}}^{m*} \end{aligned} \quad (2)$$

$$\begin{aligned} & \frac{\partial(\alpha^{m*} \rho^{m*} v^{m*})}{\partial t} + \frac{\partial(\alpha^{m*} \rho^{m*} u^{m*} v^{m*})}{\partial x} + \frac{\partial(\alpha^{m*} \rho^{m*} v^{m*} v^{m*})}{\partial y} + \frac{\partial(\alpha^{m*} \rho^{m*} w^{m*} v^{m*})}{\partial z} \\ &= \frac{\partial}{\partial x} \left[ \alpha^{m*} (\mu^{m*} + \mu_T^{m*}) \frac{\partial v^{m*}}{\partial x} \right] + \frac{\partial}{\partial y} \left[ \alpha^{m*} (\mu^{m*} + \mu_T^{m*}) \frac{\partial v^{m*}}{\partial y} \right] + \frac{\partial}{\partial z} \left[ \alpha^{m*} (\mu^{m*} + \mu_T^{m*}) \frac{\partial v^{m*}}{\partial z} \right] + S_{v^{m*}}^{m*} \end{aligned} \quad (3)$$

$$\begin{aligned} & \frac{\partial(\alpha^{m*} \rho^{m*} w^{m*})}{\partial t} + \frac{\partial(\alpha^{m*} \rho^{m*} u^{m*} w^{m*})}{\partial x} + \frac{\partial(\alpha^{m*} \rho^{m*} v^{m*} w^{m*})}{\partial y} + \frac{\partial(\alpha^{m*} \rho^{m*} w^{m*} w^{m*})}{\partial z} \\ &= \frac{\partial}{\partial x} \left[ \alpha^{m*} (\mu^{m*} + \mu_T^{m*}) \frac{\partial w^{m*}}{\partial x} \right] + \frac{\partial}{\partial y} \left[ \alpha^{m*} (\mu^{m*} + \mu_T^{m*}) \frac{\partial w^{m*}}{\partial y} \right] + \frac{\partial}{\partial z} \left[ \alpha^{m*} (\mu^{m*} + \mu_T^{m*}) \frac{\partial w^{m*}}{\partial z} \right] + S_{w^{m*}}^{m*} \end{aligned} \quad (4)$$

107 In Eqs. (1-4),  $\alpha^{m*}$ ,  $\rho^{m*}$  and  $u^{m*}$ ,  $v^{m*}$ ,  $w^{m*}$  are the volume fraction, density and flow velocity components of the  $N^{\text{th}}$  fluid  
 108 phase, respectively. Further,  $\mu_T^{m*}$  denotes turbulent viscosity of the continuous  $N^{\text{th}}$  phase and  $S_{u^{m*}}^{m*}$ ,  $S_{v^{m*}}^{m*}$ ,  $S_{w^{m*}}^{m*}$ , are the  
 109 source terms. The energy equations for the multiphase model (mixture) are:

$$\begin{aligned} & \frac{\partial(\rho^m H^m)}{\partial t} + \nabla \cdot (\rho^m U^m w^m) = \nabla \cdot (\lambda^m \Delta T^m) - \nabla \cdot q_H^{m*} + \zeta - \nabla \cdot \sum_{m^*=1}^2 (\alpha^{m*} \rho^{m*} U^{dr,m*} H^{m*}) \\ & \rho^m = \sum_{m^*=1}^2 (\alpha^{m*} \rho^{m*}), \lambda^m = \sum_{m^*=1}^2 (\alpha^{m*} \lambda^{m*}) \end{aligned} \quad (5)$$

110 Here,  $H^m$ ,  $\zeta$ ,  $U^{dr,m*}$  are enthalpy by the combination of phase-weighted, relaxation factor (functional) and drift velocity  
 111 vector of the  $N^{\text{th}}$  phase, respectively, and the latter is define as  $U^{dr,m*} = U^{m*} - U^m$ .

112 The combination of mixture velocity and enthalpy for the phase and mass-weighted variables leads to:

$$U^m = \frac{\sum_{m^*=1}^2 (\alpha^{m^*} \rho^{m^*} U^{m^*})}{\sum_{m^*=1}^2 (\alpha^{m^*} \rho^{m^*})}, H^m = \frac{\sum_{m^*=1}^2 (\alpha^{m^*} \rho^{m^*} H^{m^*})}{\sum_{m^*=1}^2 (\alpha^{m^*} \rho^{m^*})} \quad (6)$$

### 113 3.1 Inter-Phase Mass Transfer

114 In the vaporization process, if the kinetic energy of droplets and the work of viscosity term are neglected, the transfer  
115 of mass on the interface of the droplets and vapor can be reduced to [6]:

$$\Gamma^{m^*} = \frac{\sum \overline{\langle q^{m^*} \cdot \nabla_{\chi} \rangle}}{h_{fg}} \quad (7)$$

116 In Eq. (7),  $h_{fg}$  is heat transfer coefficient between the fluid and gas and  $q^{m^*}$  is the heat flux for  $N^{\text{th}}$  fluid. This equation  
117 can be defined as the net heat transport to the interface of droplet divided by the latent heat of vaporization process.

### 118 3.2 Large eddy simulation (LES)

119 In LES, the large energy-containing eddies are computed directly (within the accuracy of the computational scheme)  
120 and the small-scale structures are modeled. For the carrier bulk multiphase flow, the mathematical formulations include  
121 a continuous and discrete phase. The continuity and momentum equations used in the LES model with Favre-averaging  
122 operation are defined as follows [25]:

$$\left( \frac{\partial \rho}{\partial t} \right) + \left( \frac{\partial (\overline{\rho u_i})}{\partial x_j} \right) = 0 \quad (8)$$

$$\left( \frac{\partial (\overline{\rho u_j})}{\partial t} \right) + \left( \frac{\partial (\overline{\rho u_i u_j})}{\partial x_j} \right) = - \left( \frac{\partial p}{\partial x_i} \right) + \left( \frac{\partial \sigma_{ij}}{\partial x_j} \right) - \left( \frac{\partial \tau_{ij}}{\partial x_j} \right) + S \quad (9)$$

123 In Eq. (9),  $S$  denotes the body forces acting on the fluid. The subgrid-scale (SGS) stress tensor ( $\tau_{ij}$ ) is modeled by  
124 employing an eddy-viscosity approach

$$\tau_{ij} \approx \rho (\overline{u_i u_j} - \overline{u_i} \overline{u_j})$$

$$S_{ij} = \frac{1}{2} \left( \frac{\partial (\overline{u_j})}{\partial x_i} + \frac{\partial (\overline{u_i})}{\partial x_j} \right) \quad (10)$$

125  $S_{ij}$  is the rate of strain tensor for the resolved scale. Here, the so called 'one equation eddy-viscosity model' (OEEVM)  
126 subgrid-scale (SGS) was employed. To obtain the turbulent kinetic energy ( $K$ ), the OEEVM was solved as follows.

$$\partial (\overline{\rho k}) + \nabla \cdot (\overline{\rho k u}) = -\tau_{ij} \cdot S_{ij} + \nabla \cdot (\mu_k \nabla k) + \overline{\rho \varepsilon} \quad (11)$$

$$\varepsilon = c_3 k^{3/2} / \Delta \quad (12)$$

127 The kinetic energy in LES turbulence method is defined as:

$$\left\langle u_i \frac{\partial f_p}{\partial f_p} \right\rangle^* = u_i \frac{\partial \langle f_p \rangle^*}{\partial f_p} \quad (13)$$

$$\frac{\partial \langle f_p \rangle^*}{\partial t} + u_i \frac{\partial \langle f_p \rangle^*}{\partial x_i} + \frac{\partial}{\partial u_i} \left[ \frac{1}{\tau_p} \left( \langle U_{fi} \rangle^* - u_i \right) \langle f_p \rangle^* \right] = -\frac{1}{\tau_p} \frac{\partial \langle u_{fi}^* f_p \rangle^*}{\partial u_i}$$

128 where  $u_f^* = (U_f | C) - \langle U_f \rangle^*$ . Using Boussinesq approximation, a simple correlation for the incompressible Reynolds  
129 stress tensor is developed, which is expressed by

$$\overline{u_i' u_j'} = \frac{2}{3} k \delta_{ij} - \nu_T \left( \frac{\overline{u_i'}}{\partial x_j} + \frac{\overline{u_j'}}{\partial x_i} \right) \quad (14)$$

### 130 3.3 Droplet Evaporation Process:

131 The evaporation of droplets is modeled using [1-8]:

$$J_w = 1 \times 10^{-6} \left( 20.56 + 27.21 V_a + 6.392 V_a^2 \right) \left( 1 \times 10^{-3} (P_w - P_a) \right)^b \quad (15)$$

$$b = 1.22 - 0.19 V_a + 0.0387 V_a^2$$

132 In this regard, surface evaporation depends on  $V_a$ ,  $P_w$  and  $P_a$ , which depend on the air velocity, partial saturated vapor  
133 pressure, and partial water vapor pressure in air, respectively.

134

### 135 3.4 Droplet Merging

136 The most common way to achieve the integration of droplets is to ensure that there is an electric field where the two  
137 droplets meet. Link et al. [34] showed that there are direct relations between voltage and rate of merging. This results  
138 in oppositely charged surfaces, which will merge the particles together. Also, Chabert et al. studied the merging of  
139 individual droplets and particle pairs via electro coalescence (EC)[35]. For Newtonian and incompressible fluids at low  
140 Reynolds and Bond numbers, this process is defined as [36]:

$$\mu \nabla^2 U - \nabla P = \nabla \Theta \quad (16)$$

141 with  $\mu$  being the viscosity of fluid, U the velocity in X direction, P the total pressure and  $\Theta$  the stress field in each phase  
142 of the two-phase fluid.

### 143 3.5 Boundary Conditions

#### 144 3.5.1 Sneezing Profile

145 As shown in Fig. 2, sneezing involves a sudden change in pressure. The details of this pressure variation depends upon  
146 the person's gender, age and other physiological features. A fluid flow under the pressure trace shown in Fig.2 is ejected

147 from the mouth. The inner surface of the mouth is a wall and the throat is modelled as a pressure inlet boundary  
 148 condition. The fluid flow has a relative humidity of 75% and temperature of 35°C. Unlike previous investigations, here  
 149 the process of saliva droplet formation through passage of air over the wet surfaces of mouth and lips is fully modeled.  
 150 According to the geometry of the mouth, the applied pressure leads to an increase in the fluid velocity up to 85m/s at  
 151 the lips. The exit location of the mouth was a pressure outlet and a homogenous droplet of saliva distribution, while the  
 152 physical properties are extracted from Refs. [37, 38]. It is further clarified that the no-slip boundary condition was  
 153 applied to the fluid flow in the mouth.

### 154 3.5.2 Droplet

155 For each droplet, the shape is affected by the balance of internal and external forces. According to Ref. [39] the maximum  
 156 rate of the volume-based size distributions can be represented by [31]:

$$P_{V,i,U} = A_U \left( \frac{1}{\sqrt{2\pi\sigma_U}} \right) e^{-\frac{(\log_{10}(D_i) - \mu_U)^2}{2\sigma_U^2}} \quad (17)$$

157 In eq. (17),  $P_{V,i,U}$  is the ratio of particle diameters in size class I and  $\sigma$  is the Capillary force. In this simulation, each  
 158 droplet has two specific features a) variable surface and b) possibility of evaporation and merging.

### 159 3.6 Evaporation and Droplet Merging

160 For vaporization and condensation processes, if the kinetic energy and viscous work terms are neglected, the interfacial  
 161 mass transfer can be derived by setting  $\zeta = 0$ . According to equation (15), the mass flux due to vaporization or  
 162 condensation can be estimated with the knowledge of heat flux on each side of the interface [31]. If the fluid side heat  
 163 flux to the interface exceeds the vapor side heat flux, vaporization occurs. The reverse is true for condensation. It can  
 164 also be demonstrated that the fluid side interfacial heat flux tends to dominate the process. Using *Stefan's* correlation  
 165 and solving the surface vapor mass concentration for the interface of droplet, the concentration of mass for each phase  
 166 is [1-8].

$$C_{1M}^{2\sigma} = 1 - (1 - C_{1M}) \exp \left( \frac{D_3^2}{6\alpha_3 \rho_1 s h D_{M \rightarrow \Sigma n}} \frac{\chi_3^{1\sigma} (T_3^{1\sigma} - T_3)}{h_{M1}^{3\sigma} - h_{M3}^{3\sigma}} \right) \quad (18)$$

167 In Eqs. (18),  $C_{1M}$  mass concentration of gas component,  $h_{M1}^{3\sigma}$  is specific enthalpy for liquid (phase 1) and  $h_{M3}^{3\sigma}$  is specific  
 168 enthalpy for vapor (phase 3).

169 To calculation the partial surface pressure of the vapor, the concentration equation can be put into the body force  
 170 equations:

$$P_{M1}^{3\sigma} = p \frac{C_{M1}^{3\sigma}}{M_{M1}} \left/ \left[ \frac{C_{M1}^{3\sigma}}{M_{M1}} + \frac{1 - C_{M1}^{3\sigma}}{M_{1n}} \right] \right. \quad (19)$$

$$\begin{aligned}
F_{Drag} &= \frac{\pi}{8} \rho^f d_p^2 C_D (V_{ins}^f - V_{ins}^p) |V_{ins}^f - V_{ins}^p| \\
F_{Added} &= K_A \rho^f V_p \frac{d(V_{ins}^f - V_{ins}^p)}{dt} \\
F_{Body} &= \rho^p V_p g
\end{aligned} \tag{20}$$

171 where  $\rho^f$ ,  $d_p$ ,  $V_p$ ,  $C_D$ ,  $C_{1M}^{3\sigma}$ ,  $C_{1M}^{2\sigma}$  are the fluid density, particulate diameter, volume of the second phase for a spherical  
172 particulate, partial surface pressure of the vapor and surface vapor mass concentration, respectively. Further,  $V_{ins}^p$  is  
173 volume of the second phase (the initial state) and  $V_{ins}^f$  denotes the volume of fluid (the initial state).

174 Due to the complexity of sneezing process, here, a multi-layer flow solver was used. The domain was divided into four  
175 parts. In the first part, the internal airflow in the throat and mouth was modeled by employing a single phase RANS, K-  
176 epsilon model considering the movement within the oral environment. In this part, a polyhedral mesh structure and  
177 the coupling of the SIMPLE velocity and pressure equations were used. Since the configuration involves a single-phase  
178 mode at the inlet along with saliva over the entire inner surface of the mouth, a volume-of fluid (VOF) methodology was  
179 employed to model the multiphase flow in that region. This renders a hybrid model, which starts as a single-phase flow  
180 and gradually turns into a two-phase flow.

181 In the second part, starting from the mouth and extending for 1 meter, LES was utilized to model the spray and  
182 dispersion of droplets of saliva. Due to the relatively high velocity of the flow in this section and the presence of vortices,  
183 a full structure grid generation has been developed. Included in the model is evaporation and heat transfer within the  
184 droplet and the possibility of droplets merging. It is essential to note that unlike most existing studies on modeling of  
185 sneezing, here no model of spray or ejector was used. Instead, the entire process of two-phase flow formation was  
186 replicated. Liquid droplets were precisely modeled in the space of one meter from the face of the sneezing person. The  
187 droplets leaving the mouth cover a wide range of diameter from one to one thousand microns. The statistical  
188 distribution of these particles at the moment of exiting the mouth is quite uniform. In the LES region, the second-order  
189 precision and QUICK solution model were applied. Also in this area, due to the geometric deformation of the droplets  
190 and their movement, an adaptive grid generation was used for each particle movement. The time step was adaptive by  
191 location and a time step of 0.0001s was considered as the basis.

### 192 3.7 Concentration and Particle Diameter Measurement (PDM)

193 Fig. 3 illustrates the method applied to calculate the average value of the droplets in each time step. Based on this, one  
194 computational domain for each droplet around the virtual center of mass was considered. This computational domain  
195 was fitted to the surface of droplet. The fitting process was based on the adaptive grid generation. A number of vertical  
196 vectors on the surface were drawn at any point with the same distribution on the surface, the number of which  
197 increased or decreased depending on the particle diameter. The average value of droplet diameter was obtained at any  
198 given time in all ranges. The values calculated at each time step were then averaged from all three axes. The amount of  
199 virus transmitted by each droplet is directly related to the particle diameter. Therefore, the study of changes and

200 classification of droplets based on their average diameter is an important part of calculating the distribution of droplets  
201 in the range of 1 to 1000 microns. This specific model examines the diameter changes at each time step, which vary by  
202 the external and internal forces and evaporation, and provides an ability to statistically evaluate the diameter of the  
203 droplets. The developed scheme further offers the ability to calculate the number of particles in a constant volume through  
204 applying an image processing technique.

### 205 **3.8 Validation**

206 Extensive tests confirmed the grid independency of the simulations. Further, a comparison between the current  
207 numerical results and those from several well-established computational models and empirical correlations have been  
208 presented in Fig. 4. An excellent agreement is evident confirming validity of the numerical simulations.

## 209 **4. Artificial Intelligence**

210 To predict of the concentration and velocity, a Multi-Input Multi-Output (MIMO) model is developed. In each  
211 experiment, several inputs including time, concentration and velocity are given to the model to calculate concentration  
212 outputs. The number of input samples in each experiment is about 1240. For prediction, a Deep Neural Network (DNN)  
213 regression with a number of input, hidden and output layers was constructed [43]. One superiority of this model is  
214 achieving high accuracy on complex data. One of its main challenges is the existence of a weak structural theory [44].  
215 In other words, there is no certain theory for the arrangement of elements in a network. Often, the model is studied  
216 experimentally and by applying some techniques such as changing the number of layers and neurons and testing  
217 different activation functions the accuracy of the model is improved. The sequential models used in this paper have  
218 been developed by importing sequential functions from the Keras library of Python. By using the Dense function of the  
219 Keras library, 5 layers have been inserted to the network. The first layer is used as the input layer to receive attributes  
220 values. Model attributes are: time, location, pressure, temperature and density. In the proposed model, three hidden  
221 layers are used, which include 30, 20 and 15 neurons, respectively. The number of neurons and the type of activation  
222 functions were selected by several experiments.

223 Of course, in selecting the appropriate structure for the network, it is useful to use the proposed structures in  
224 models that have already been used for DNN regression. The ReLU activation function is used for the neurons of hidden  
225 layer, which is one of the most widely utilized and simplest nonlinear activation functions. The two advantages of this  
226 function are that it is not saturated with a large number of inputs and the errors are simply back propagate [43]. The  
227 last layer of the network is the output layer, which contains some neurons. These neurons return the result of the  
228 prediction of concentration and velocity. The defect of the ReLU activation function is that it only takes values for values  
229 greater than zero. Thus, the Sigmoid activation function is used in the output layer. Other settings made on the model  
230 are the selection of epoch value and batch size. An epoch is a count of the number of times all training data are used  
231 once to update neural weights. For batch training, all training samples go through the training algorithm simultaneously  
232 at an epoch before the weights are updated. The model weights is updated at the end of each epoch and the batch size.  
233 Adam optimizer is also used to calculate the adaptive learning rate for each parameter. This optimizer has been utilized  
234 to update the neuron weights of hidden layer.

235 Finally, the steps of creating the proposed model are presented. At first, the provided dataset is loaded. Then, the  
 236 data preprocessing is done, which includes data normalization. Then, the sequential model is created. Input, hidden,  
 237 and output layers are created using the ReLU and Sigmoid activation functions. Afterwards, model compilation is done  
 238 using Adam optimizer. The epoch value and batch size are determined for the model. Subsequently, the concentration  
 239 and velocity prediction is done with the model. Finally, the model is evaluated. Tensor flow has been used as a backend  
 240 to create a predictive model based on deep neural network. It is a library written for high-performance numerical  
 241 calculations in Python. The Sequential Model API has also been developed and evaluated with Keras and Python3  
 242 libraries. Keras is a Python library developed for deep learning. The Sequential model API is utilized to create a model  
 243 for predicting the concentration and velocity and to which the model layers are added. Also, the Keras Regressor was  
 244 used to evaluate the model. Performance evaluation was performed using tenfold cross-validation. In this method, the  
 245 samples are divided into 10 categories. In each step, 9 categories are used to train the model and 1 category is used to  
 246 test the model. The epoch and batch size values are set to 200 and 5, respectively.

247 The accuracy of the model is calculated with the criteria of Mean Square Error (MSE) and Mean Absolute Error  
 248 (MAE). These criteria are calculated as follow:

$$\text{MAE} = \frac{\sum_{i=1}^n |y_i - t_i|}{n} \quad (24)$$

$$\text{MSE} = \frac{\sum_{i=1}^n (y_i - t_i)^2}{n} \quad (25)$$

249 in which  $y_i$  and  $t_i$  are prediction and target values, respectively and  $n$  is the total number of data points. Several  
 250 nonlinear models have been evaluated to select the appropriate model for concentration and velocity prediction. For  
 251 this purpose, several well-known neural networks including Multi-Layer Perceptron (MLP), Support Vector Regression  
 252 (SVR) and Radial Basis Function (RBF) are compared to DNN. The results of this comparisons are shown in Table 2. In  
 253 this evaluation, two criteria 1 and 2 have been considered for each network. Based on the results, the DNN with a  
 254 significant difference represents a better accuracy than other models. After that, RBF can be used as an appropriate  
 255 choice to predict concentration and velocity.

256 Table 2: Mean Square Error (MSE) and Mean Absolute Error (MAE) to predict concentration for various potential  
 257 models.

Mean Error	Various potential models							
	DNN	CFD error (%)	MLP	CFD error (%)	SVR	CFD error (%)	RBF	CFD error (%)
MAE	6.72	0.154	2.92	12.36	1.03	8.45	1.72	0.369
	$\times 10^{-6}$		$\times 10^{-5}$		$\times 10^{-5}$		$\times 10^{-5}$	
MSE	3.62	0.266	1.82	37.85	4.13	5.44	9.10	1.254
	$\times 10^{-10}$		$\times 10^{-8}$		$\times 10^{-9}$		$\times 10^{-10}$	

258

## 259 **5. Characteristics of sneezing process**

260 In the sneezing process, the droplets with larger diameter and thus heavier weight settle under gravity and deposit on  
261 the surfaces. The rest of droplets are dispersed at longer distances from the sneezing point. This longitudinal distance  
262 depends on the ambient air temperature and the initial velocity of the droplets. Therefore, the spatiotemporal  
263 distribution of droplets generated by sneezing is dominated by the environmental parameters and the sneezing  
264 parameters. It is known that the concentration of droplets and the exposure time with the contaminated environment  
265 are important factors in determining the transmission risk of COVID-19 [1, 11, 39, 45, 46]. Hence, in this section the  
266 effects of pertinent parameters influencing the dispersion of particles are examined.

267 Fig. 5 shows the parameters that characterize the employed sneezing model. These parameters were extracted  
268 from the latest literature on the distribution of sneezing droplets [1-6]. In general, the dispersion process of the sneezing  
269 droplets leads to the formation of three different regions. These are separable based on the rate of deposition and are  
270 marked in different colors in Fig. 5. In the red zone, particles with large mass fell quickly and hit the ground at a short  
271 distance from the sneezing person. The percentage of these particles is low. Yet, due to their considerable mass, they  
272 can carry a large amount of virus. Conduction of image processing on the numerical results revealed that distribution  
273 pattern of this zone is different for each person. The flow velocity in this zone varies between 50 and 100 m/s [1-3]. The  
274 second zone, which has a lower concentration of particles compared to the first zone, is marked in orange in Fig. 5. This  
275 area, as presented in the following sections, has the largest particle diameter relative to the longitudinal distance and  
276 thus the highest risk of transmission. Zone three, marked in blue in Fig. 5, is of particular importance. Although this  
277 zone has a low density of particles, it is a very large and hence important area. The extent of this zone is because of the  
278 suspension of particles, which brings down their sedimentation rate and enables them to survive for a long time. Most  
279 importantly, these suspended particles can readily travel with the air flow and spread the virus vastly.

## 280 **6. Results and discussion**

### 281 **6.1. Sneezing dynamics**

282 Sneezing is a fully automated process and a natural reaction to remove any contaminants from the lungs. This process  
283 travels as a pressure wave from the lungs to the mouth [13, 45, 47]. This high-pressure flow, once expelled from human  
284 mouth and nose, distributes saliva in the form of droplets in the environment. The generated flow changes the size and  
285 diameter of these droplets. Modeling of these changes during the sneezing process is one of the most important features  
286 of the current work. Previous studies often used particle distribution models based on the distribution of the spherical  
287 particles [39, 48-50]. This prevents examination of the changes in droplet diameter during the sneezing process.  
288 Further, since movement within the air-fluid causes deformation of the droplets, the drag force caused by the  
289 deformation is not constant and this has a significant effect on the droplet distribution.

290 Fig. 6 shows a typical view of the process of breaking droplets during the sneezing process in the vicinity of human  
291 mouth. This analysis was conducted by image processing applied on the LES results. It shows that large droplets fall  
292 into small particles within a short distance. It also shows that the concentration of saliva in the unit volume of the  
293 densely packed area is much higher than other areas. Figure 6 further indicates that the break and splitting of large

294 droplets due to the internal forces and drag forces reduce the concentration in the constant volume. This, in turn, leads  
295 to the expansion of the contaminated space with sneezing droplets. The spread of virus in the process of sneezing  
296 depends on various parameters such as speed and direction, as well as the virus concentration in saliva. Further, it has  
297 been shown that the physical properties of saliva varies amongst different people [37, 38].

298 The statistics of droplet diameter is an essential outcome of the current analysis. It is already evident that there  
299 exists a correlation between the droplet diameter and the possibility of infection transmission [1, 11-13]. The changes  
300 in diameter depends on the evaporation rate, flow field and the physical properties of saliva. Figure 7 shows the  
301 statistical distribution of droplets based on the average diameter at two different instances of time. The results clearly  
302 show that the droplet diameter is strongly time dependent. Changes in the droplet diameter directly influence the  
303 droplet distribution. As such, there is a direct relation between droplet diameter and deposition rate. Also, increasing  
304 the rate of evaporation may help reducing the concentration of droplets near the sneezing person. Particles with  
305 diameters of 1 to 250 micrometers are more likely to become suspended. These particles are not transported by air  
306 flow to far distances from the sneezing person.

307 As shown in Fig.7, it is also clear that the distribution of particles in the transversal direction within the range of 1  
308 to 100 microns is the greatest. The issue of sneezing and its spread in the investigated environment (inside the bus) has  
309 some unique features. First, the infected person sneezes at the end of the bus and the droplets are spread out by natural  
310 dispersion as well as the air flow set by the ventilation system. Second, the ambient temperature influences the particle  
311 density by altering the evaporation rate. Further, it has been shown that the evaporation rate has an inverse relationship  
312 with the droplet diameter and decreases with increasing the droplet diameter [14]. Fig.7 further shows the effects of  
313 temporal changes on different droplet diameters. It is important to note that during the sneezing process, the time and  
314 size of the droplets play a major role in the spread of the virus.

## 315 **6.2. Droplet Dispersion in the bus-CFD Approach**

316 In general, there are two important factors dominating the probability of infection: exposure time and concentration of  
317 virus [51-53]. Sneezing process involves a wide range of droplet diameter with different velocity. According to the  
318 weight and diameter, each particle has a specific deposition velocity. It follows that the spatial analysis of particle  
319 diameter and concentration can help assessing the risk of infection.

320 Figure 8 shows the distribution of droplets within the range of two meters from the person. The classification of  
321 regions in Fig. 8a is on the basis of the downward velocity of the droplets which drives the sedimentation process. A  
322 volume of 2 m<sup>3</sup> was considered in front of the sneezing person and a series of image processing techniques were  
323 employed to identify the droplet velocity. This led to identification of three spatial regions. In the green region, the  
324 ensemble average of the downward velocity of droplets is less than 0.001m/s. This quantity increases to 0.1 m/s and  
325 0.5 m/s in the blue and brown regions. As shown in Fig. 8a, the affected area of sneezing droplets can generally be  
326 divided into three parts based on concentrations. In this figure, drawn along the vertical and horizontal axis of the bus  
327 geometry, it is clear that the sneezing person disperses a different percentage of droplets in each area. The path lines  
328 have been shown for a selected number of droplets. Most of droplets in the low-density region are those with diameters

329 between 1 to 25 microns, while the droplets with a diameter of 113 to 225 microns are most common in the medium  
330 density section. As stated previously, the deposition rate of every droplet is directly related to the diameter, therefore  
331 it is expected that smaller diameter droplets would be dispersed farther away from the sneezing person. It is observed  
332 that in the area with high density, particles of 510 to 700 microns are most common. The deposition rate of the particles  
333 and the time they remain suspended depend directly on the particle diameter. Regardless of the resultant forces, the  
334 droplet diameter has a direct effect on the deposition time. Also, due to the changes in diameter along the longitudinal  
335 direction of the bus, it can be stated that the droplet deposition time increases directly. Expectedly, heavy droplets  
336 deposit at a faster rate than those with a smaller mass.

337 Figure 8b shows the distribution of droplets from the top view. It is clear that the pattern of transverse  
338 distribution varies according to the location of the individual as well as other environmental parameters. Heavy  
339 particles are scattered quickly and in front of the sneezing person. Due to their high mass and inertia, these particles  
340 have less deviation from the axial direction of sneezing. This figure further shows that in the areas with low density  
341 (green) particles are more prone to be affected by the suction and ventilation system of the bus.

342 Figure 8b, depicts the top view of droplet distribution in the bus. It is inferred from this figure that the cross-  
343 section of the particle transport may change the areas of accumulation of heavy particles. The diffusion environment  
344 varies based on the position in the three-dimensional space, the distance between the droplet and the sneezing location  
345 for different models. The results further indicate that according to the particle mass, the path of a particle can be  
346 different. Also, by comparing Figs. 8a and 8b, it is clear that the process of transfer and deposition of particles is strongly  
347 dependent on the time and environmental conditions. The process of distributing the sneezing particles in the bus is  
348 statistically affected by the environmental conditions.

349 The deposition process and distribution of droplets were studied computationally up to 2 m from the sneezing  
350 person. Figure 9 shows the contours of droplet concentration drawn on three planes at the distances of 0.5, 1 and 2m  
351 from the sneezing person. In order to compare the droplet concentration, Fig. 9 is based on the percentage of droplets  
352 per unit volume (number of particles or droplets in standard control volume by considering the evaporated mass of  
353 droplets).

$$concentration(\%) = \left( \frac{\text{number of particle}(selected\ range)}{\text{number of particle}(selected\ range)in\ t = 0.1s\ in\ C.V\ close\ to\ the\ face} \right) \quad (26)$$

354

355 The results show that the droplet diffusion is directly related to the droplet size. It is known that increasing the  
356 diameter of the droplets modifies the distribution model and alters the maximum deposition location. Figure 9 shows  
357 that for the droplets with diameters between 1 to 250 microns, there exists a very small amount of sedimentation. That  
358 is to say that the droplets of this size practically do not sediment and remain suspended and therefore can be easily  
359 transferred along the bus. These droplets are the primary suspect of the infection parameter. As an important point,  
360 Fig. 9 further shows that the ventilation system can reduce the droplet concentration by removing the droplets. Some

361 of these droplets, with the diameters between 250-500 microns, may deposit. Other droplets can be still transferred  
362 along the bus and contribute to transmission of the virus.

363 By increasing the droplet diameter, the deposition rate is expected to increase. According to Fig. 10, the droplets  
364 with diameters of 500-750 micron can deposit quickly within a short distance from the sneezing person. The results  
365 show that for this range of droplet diameter, there is a large concentration gradient along the bus. Overall, the  
366 simulations indicate that the droplets with diameters of 1 to 250 microns have the highest diffusion speed amongst all  
367 generated droplets. This is because of their small size and their ability to be suspended in air. According to Fig. 10, for  
368 the droplets with the diameter of 1 to 250 microns at a distance of two meters, the velocity changes are greater than  
369 those of other droplets. Also, the results in Fig. 10 show that with increasing the diameter of the droplets, their average  
370 velocity decreases by a factor three, which clearly shows the importance of spreading the droplets with small diameters.

### 371 **6.3. Droplet Dispersion in the bus-AI Approach**

372 The last section demonstrated that the computational model can provide an insight into the spread of virus in the  
373 selected environment (bus). Nonetheless, the computational burden of the model poses a serious practical issue. Rapid  
374 computation for risk assessment purposes is almost impossible and therefore alternative approaches should be sought  
375 for the prediction of particle distribution. The use of AI can reduce the computational cost of the analysis and increase  
376 the processing speed up to almost 100 times. Here, the computationally generated data are used to train an AI tool (see  
377 Section 4) that predicts the temporal and spatial evolution of the particle distribution in the bus. In Fig. 11, the results  
378 obtained from the AI model and those produced through numerical simulations are presented for four different areas.  
379 A comparison between the two sets of data confirms the accuracy of the developed AI tool to predict the droplet  
380 distribution. The excellent agreement between the computationally and AI generated data means that artificial  
381 intelligence can predict the concentration in the entire volume of the bus. As shown in Figure 10, these values are for  
382 the middle plane of the bus and the midline on this plane. It is important to note that with increasing the computational  
383 accuracy in region 1, fewer changes for the data obtained from artificial intelligence are encountered.

384 In Fig. 12, the concentration of particles has been plotted based on their diameter distribution in the whole volume  
385 of the bus over 9 different parallel planes with increasing distance from the sneezing person. It is recalled that  
386 computational modeling was performed only for the first two meters away from the sneezing person and the rest of the  
387 domain was predicted by the AI tool. In keeping with the computational result, the AI results show that smaller  
388 diameter particles can propagate widely throughout the bus. As farther distance is taken from the sneezing person, a  
389 decrease in the concentration of particles and a gradual deposition of particles in different parts are observed. The data  
390 presented in this figure are based on the Aceh emission analysis model at the distance of two meters. In producing those  
391 data, the maximum particle density was plotted on each plane for 10 seconds. Also, the presence of ventilation in the  
392 bus and the upper part of the passengers' heads can change the pattern of the particle distribution. It is further observed  
393 that the particles with small diameters are readily transported throughout the bus. Also, heavy particles evaporate and  
394 turn into smaller particles. The presence of flow obstacles such as passenger seats impart a major effect on the  
395 distribution and suspension of particles as well as sedimentation of the settling particles. This is because the air flow is  
396 very small in between the seats. Thus, the sedimentation model and the deposition of particles are modified in the space

397 between the seats. The results show that artificial intelligence has the capability of predicting the temporal and spatial  
398 distribution of particles in the complex and highly varying environment of the bus. Since AI analysis is much faster  
399 (around 100 times) than the corresponding computational analysis, it can be used in practice to evaluate the spread of  
400 droplets and the associated risk of infection. An overall view of the temporal spread of droplets within the bus can be  
401 found in the companion animation file. In there, the data on the first 2 meters from the sneezing passenger have been  
402 extracted from the CFD analysis and the spread of droplets in the rest of the bus was predicted by the AI tool.

## 403 **7. Conclusions**

404 Protection against COVID-19 and establishment of relevant risk assessment schemes are currently central to the health  
405 and wellbeing of the society. Understanding the patterns of virus spread and their pertinent parameters are amongst  
406 the key issues raised in the recent months. Importantly, there is a pressing need for the quick assessment of  
407 transmission risk in indoor environments with large occupancy. In particular, public transport has been identified as  
408 one of the main routes to virus transmission. This poses a major challenge on the conventional simulations based on  
409 computational fluid dynamics, as the required computational time makes them impractical for risk assessment. To  
410 address this issue, an attempt was made to provide a novel approach to the prediction of droplet distributions set by  
411 sneezing of an infected person in a bus. This was based on the high fidelity computation of the droplets formation during  
412 the sneezing process followed by the droplets dispersion in the domain up to 2m away from the sneezing person. The  
413 processes of droplets formation and spread were modeled through applying the volume of fluid and LES methodologies  
414 to the person's mouth and the immediate surroundings. The resultant computational data were then used to develop  
415 an AI-based tool capable of predicting the evolution of droplet distribution in the entire volume of the bus. It was shown  
416 that while the AI-based approach reduces the computational time most significantly (~100 times), it offers an excellent  
417 accuracy. Hence, the developed combined scheme on the basis of CFD and AI is deemed suitable for practical risk  
418 assessments.

419 In addition to this, the following physical outcomes emerged from this work.

- 420 1- The boundary conditions have substantial effects on the droplet dispersion. The ambient velocity and initial  
421 speed of droplets can widen the septic zone.
- 422 2- The droplet diameter dominates the dispersion process. The droplets with smaller diameters (less than 250  
423 microns) are very likely to remain suspended in air and thus be transferred to other parts of the environment.
- 424 3- The results indicate that about 59% of the initial droplet will be deposited in the first 2 meters away from the  
425 sneezing person. The droplets with diameters between 500 and 1000 microns are most likely to fall and hit the  
426 ground within this distance.
- 427 4- The concentration of droplets could decline to 87% in the first 3 meters. Nonetheless, this process is heavily  
428 affected by the ambient temperature and airflow velocity.

## 429 **Acknowledgment**

430 The first author (M. Mesgarpour) acknowledges Postdoctoral Fellowship from KMUTT. S. Wongwises acknowledges  
431 the support provided by the "Research Chair Grant" National Science and Technology Development Agency

432 (NSTDA), and King Mongkut's University of Technology Thonburi through the "KMUTT 55<sup>th</sup> Anniversary  
433 Commemorative Fluid. N. Karimi acknowledges the financial support by the Engineering and Physical Science  
434 Research Council through the grant number EP/V036777/1 Risk Evaluation Fast Intelligent Tool (RELIANT) for  
435 COVID 19.

## 436 Reference

- 437 1. Chen, L.-D., *Effects of Ambient Temperature and Humidity on Droplet Lifetime—A Perspective of Exhalation Sneeze Droplets with*  
438 *COVID-19 Virus Transmission*. International Journal of Hygiene and Environmental Health, 2020: p. 113568.
- 439 2. Meccariello, G. and O. Gallo, *What ENT doctors should know about COVID-19 contagion risks*. Authorea Preprints, 2020.
- 440 3. Diwan, S.S., et al., *Understanding Transmission Dynamics of COVID-19-Type Infections by Direct Numerical Simulations of*  
441 *Cough/Sneeze Flows*. Transactions of the Indian National Academy of Engineering, 2020: p. 1.
- 442 4. Rockett, R.J., et al., *Revealing COVID-19 transmission in Australia by SARS-CoV-2 genome sequencing and agent-based modeling*.  
443 *Nature medicine*, 2020. **26**(9): p. 1398-1404.
- 444 5. Enserink, M. and K. Kupferschmidt, *With COVID-19, modeling takes on life and death importance*. 2020, American Association for  
445 the Advancement of Science.
- 446 6. Ivorra, B., et al., *Mathematical modeling of the spread of the coronavirus disease 2019 (COVID-19) taking into account the*  
447 *undetected infections. The case of China*. Communications in nonlinear science and numerical simulation, 2020. **88**: p. 105303.
- 448 7. Chaudhuri, S., et al., *Modeling the role of respiratory droplets in Covid-19 type pandemics*. Physics of Fluids, 2020. **32**(6): p. 063309.
- 449 8. Abuhegazy, M., et al., *Numerical investigation of aerosol transport in a classroom with relevance to COVID-19*. Physics of Fluids,  
450 2020. **32**(10): p. 103311.
- 451 9. Hassani, K. and S. Khorramymehr, *In silico investigation of sneezing in a full real human upper airway using computational fluid*  
452 *dynamics method*. Computer methods and programs in biomedicine, 2019. **177**: p. 203-209.
- 453 10. Singh, R.K. and S.N. Tripathi, *Application of National Aerosol Facility (NAF) in Designing of a Ventilation System for Isolation Rooms*  
454 *to Minimize Interpersonal Exposure of Sneezing/Coughing*. Transactions of the Indian National Academy of Engineering, 2020: p.  
455 1.
- 456 11. Kotb, H. and E.E. Khalil. *Impact of Sneezed and Coughed Droplets Produced from a Moving Passenger on Other Passengers inside*  
457 *Aircraft Cabins*. in *AIAA Propulsion and Energy 2020 Forum*. 2020.
- 458 12. Busco, G., et al., *Sneezing and asymptomatic virus transmission*. Physics of Fluids, 2020. **32**(7): p. 073309.
- 459 13. Li, H., et al., *Dispersion of evaporating cough droplets in tropical outdoor environment*. Physics of Fluids, 2020. **32**(11): p. 113301.
- 460 14. Hasan, A., *Tracking the Flu Virus in a Room Mechanical Ventilation Using CFD Tools and Effective Disinfection of an HVAC System*.  
461 *International Journal of Air-Conditioning and Refrigeration*, 2020. **28**(02): p. 2050019.
- 462 15. Verma, S., M. Dhanak, and J. Frankenfield, *Visualizing droplet dispersal for face shields and masks with exhalation valves*. Physics  
463 of Fluids, 2020. **32**(9): p. 091701.
- 464 16. Mu, L., et al., *Unsteady CFD simulation on ash particle deposition and removal characteristics in tube banks: Focusing on particle*  
465 *diameter, flow velocity, and temperature*. Journal of the Energy Institute, 2020.
- 466 17. Hendry, J.R., J.G. Lee, and M.J. Batrum, *CFD model of fluid flow and particle deposition during cryogenic condensation*. Chemical  
467 *Engineering Research and Design*, 2019. **143**: p. 201-214.
- 468 18. Kim, Y., et al., *CFD modelling of air and particle flows in different airway models*. Journal of Aerosol Science, 2019. **134**: p. 14-28.
- 469 19. Lu, H. and L. Lu, *CFD investigation on particle deposition in aligned and staggered ribbed duct air flows*. Applied Thermal  
470 *Engineering*, 2016. **93**: p. 697-706.
- 471 20. Seyfi, S., B. Mirzayi, and H. Seyyedbagheri, *CFD modeling of black powder particles deposition in 3D 90-degree bend of natural*  
472 *gas pipelines*. Journal of Natural Gas Science and Engineering, 2020: p. 103330.
- 473 21. Song, J., et al., *Experimental and CFD study of particle deposition on the outer surface of vortex finder of a cyclone separator*.  
474 *Chemical Engineering Journal*, 2017. **309**: p. 249-262.
- 475 22. Dutta, R., et al., *CFD Guided Optimization of Nose-to-Lung Aerosol Delivery in Adults: Effects of Inhalation Waveforms and*  
476 *Synchronized Aerosol Delivery*. Pharmaceutical Research, 2020. **37**(10): p. 1-18.
- 477 23. Ivanov, M. and S. Mijorski, *Assessment of Transient CFD Techniques for Virtual Thermal Manikins' Breathing Simulations*.  
478 *Environmental Processes*, 2019. **6**(1): p. 241-251.
- 479 24. Huang, F., et al., *Role of CFD based in silico modelling in establishing an in vitro-in vivo correlation of aerosol deposition in the*  
480 *respiratory tract*. Advanced Drug Delivery Reviews, 2020.
- 481 25. Vuorinen, V., et al., *Modelling aerosol transport and virus exposure with numerical simulations in relation to SARS-CoV-2*  
482 *transmission by inhalation indoors*. Safety Science, 2020. **130**: p. 104866.
- 483 26. Yang, X., et al., *Understanding the ash deposition formation in Zhundong lignite combustion through dynamic CFD modelling*  
484 *analysis*. Fuel, 2017. **194**: p. 533-543.
- 485 27. Christodoulou, L., et al., *State prediction of an entropy wave advecting through a turbulent channel flow*. Journal of Fluid  
486 *Mechanics*, 2020. **882**.

- 487 28. Alizadeh, R., et al., *Application of Machine Learning to Investigation of Heat and Mass Transfer Over a Cylinder Surrounded by*  
488 *Porous Media-The Radial Basic Function Network*. Journal of Energy Resources Technology, 2020: p. 1-18.
- 489 29. Abad, J.M.N., et al., *Analysis of transport processes in a reacting flow of hybrid nanofluid around a bluff-body embedded in porous*  
490 *media using artificial neural network and particle swarm optimization*. Journal of Molecular Liquids, 2020: p. 113492.
- 491 30. Alizadeh, R., et al., *A machine learning approach to predicting the heat convection and thermodynamics of an external flow of*  
492 *hybrid nanofluid*. Journal of Energy Resources Technology, 2020: p. 1-22.
- 493 31. Yeoh, G.H. and J. Tu, *Computational techniques for multiphase flows*. 2019: Butterworth-Heinemann.
- 494 32. Kolev, N.I. and N.I. Kolev, *Multiphase flow dynamics: Fundamentals*. Vol. 1. 2007: Springer.
- 495 33. Crowe, C.T., et al., *Multiphase flows with droplets and particles*. 2011: CRC press.
- 496 34. Link, D.R., et al., *Electric control of droplets in microfluidic devices*. Angewandte Chemie International Edition, 2006. **45**(16): p.  
497 2556-2560.
- 498 35. Chabert, M., K.D. Dorfman, and J.L. Viovy, *Droplet fusion by alternating current (AC) field electrocoalescence in microchannels*.  
499 *Electrophoresis*, 2005. **26**(19): p. 3706-3715.
- 500 36. Niu, X., et al., *Pillar-induced droplet merging in microfluidic circuits*. Lab on a Chip, 2008. **8**(11): p. 1837-1841.
- 501 37. Ericsson, Y. and L. Stjernström, *Saliva viscosity measurements*. Oral Surgery, Oral Medicine, Oral Pathology, 1951. **4**(11): p. 1465-  
502 1474.
- 503 38. Briedis, D., M. Moutrie, and R. Balmer, *A study of the shear viscosity of human whole saliva*. Rheologica Acta, 1980. **19**(3): p. 365-  
504 374.
- 505 39. Han, Z., W. Weng, and Q. Huang, *Characterizations of particle size distribution of the droplets exhaled by sneeze*. Journal of the  
506 Royal Society Interface, 2013. **10**(88): p. 20130560.
- 507 40. Gupta, J., C.H. Lin, and Q. Chen, *Flow dynamics and characterization of a cough*. Indoor air, 2009. **19**(6): p. 517-525.
- 508 41. Ranz, W. and W.R. Marshall, *Evaporation from drops*. Chem. eng. prog, 1952. **48**(3): p. 141-146.
- 509 42. Hamey, P., *The evaporation of airborne droplets*. 1982.
- 510 43. Schmidt-Hieber, Johannes. "Nonparametric regression using deep neural networks with ReLU activation function." *Annals of*  
511 *Statistics* 48, no. 4 (2020): 1875-1897.
- 512 44. Du, Jun, and Yong Xu. "Hierarchical deep neural network for multivariate regression." *Pattern Recognition* 63 (2017): 149-157.
- 513 45. Burke, W., *Why do we sneeze? Medical hypotheses*, 2012. **78**(4): p. 502-504.
- 514 46. Pendar, M.-R. and J.C. Páscoa, *Numerical modeling of the distribution of virus carrying saliva droplets during sneeze and cough*.  
515 *Physics of Fluids*, 2020. **32**(8): p. 083305.
- 516 47. Kitta, T., et al., *The effect of ovariectomy on urethral continence mechanisms during sneeze reflex in middle-aged versus young*  
517 *adult rats*. Neurourology and Urodynamics, 2016. **35**(1): p. 122-127.
- 518 48. Dan, H.-C., et al., *DEM-aided method for predicting the hydraulic properties with particle-size distribution of porous media*.  
519 *Engineering Computations*, 2019.
- 520 49. Song, S., et al., *Particle-scale modelling of fluid velocity distribution near the particles surface in sand filtration*. Water Research,  
521 2020: p. 115758.
- 522 50. Jiang, M., et al., *The influence of particle-size distribution on critical state behavior of spherical and non-spherical particle*  
523 *assemblies*. Granular Matter, 2018. **20**(4): p. 80.
- 524 51. Ueba, O., *Respiratory syncytial virus. I. Concentration and purification of the infectious virus*. Acta medica okayama, 1978. **32**(4).
- 525 52. Gerba, C.P., *Applied and theoretical aspects of virus adsorption to surfaces*. Advances in applied microbiology, 1984. **30**: p. 133-  
526 168.
- 527 53. Jang, Y., et al., *Evaluation of changes induced by temperature, contact time, and surface in the efficacies of disinfectants against*  
528 *avian influenza virus*. Poultry science, 2014. **93**(1): p. 70-76.

529

530

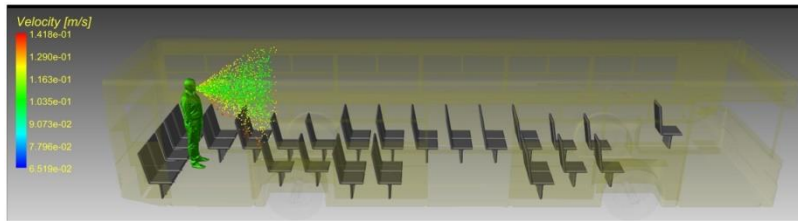
531

532

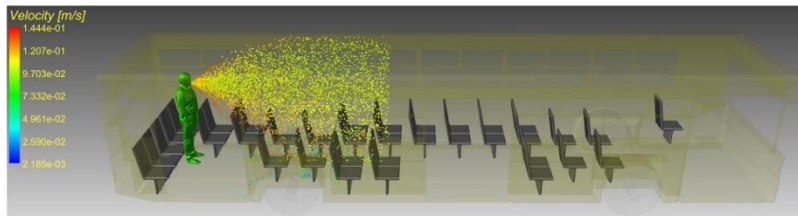
533

534

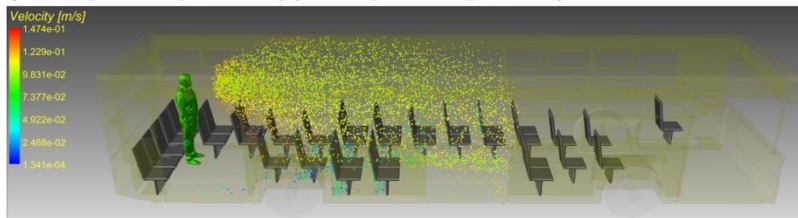
535



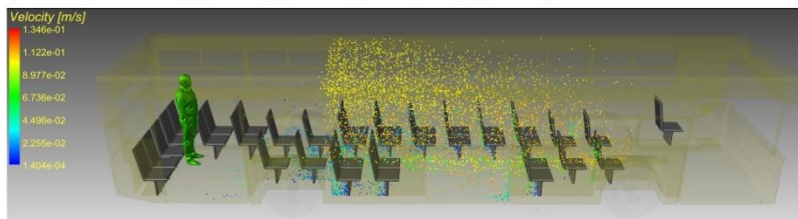
$t = 0.1s, T = 20^\circ C,$   
 $(20\mu m < d_p < 100\mu m, N_{particle} \sim 580K), (100\mu m < d_p < 300\mu m, N_{particle} \sim 919K)$   
 $(300\mu m < d_p < 500\mu m, N_{particle} = 1,020K), (500\mu m < d_p < 1000\mu m, N_{particle} = 2,856K)$



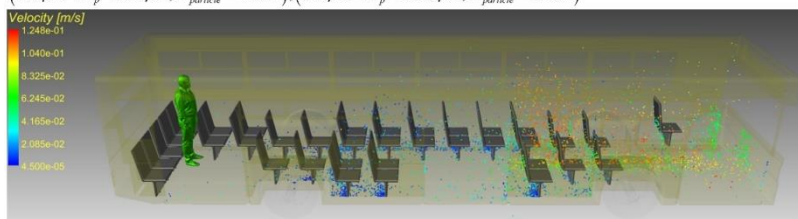
$t = 0.5s, T = 20^\circ C,$   
 $(20\mu m < d_p < 100\mu m, N_{particle} \sim 1,720K), (100\mu m < d_p < 300\mu m, N_{particle} \sim 1,349K)$   
 $(300\mu m < d_p < 500\mu m, N_{particle} = 1,065K), (500\mu m < d_p < 1000\mu m, N_{particle} = 866K)$



$t = 0.9s, T = 20^\circ C,$   
 $(20\mu m < d_p < 100\mu m, N_{particle} \sim 1,980K), (100\mu m < d_p < 300\mu m, N_{particle} \sim 1,469K)$   
 $(300\mu m < d_p < 500\mu m, N_{particle} = 945K), (500\mu m < d_p < 1000\mu m, N_{particle} = 606K)$

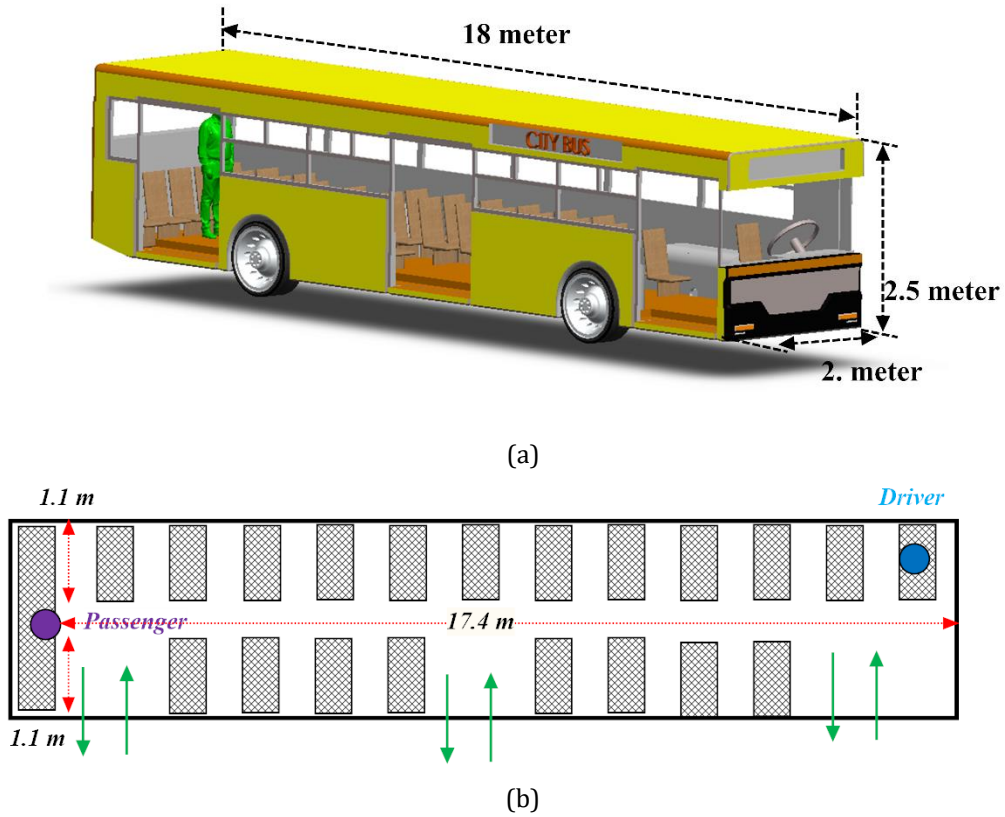


$t = 3.0s, T = 20^\circ C,$   
 $(20\mu m < d_p < 100\mu m, N_{particle} \sim 2,935K), (100\mu m < d_p < 300\mu m, N_{particle} \sim 1042K)$   
 $(300\mu m < d_p < 500\mu m, N_{particle} = 680K), (500\mu m < d_p < 1000\mu m, N_{particle} = 343K)$

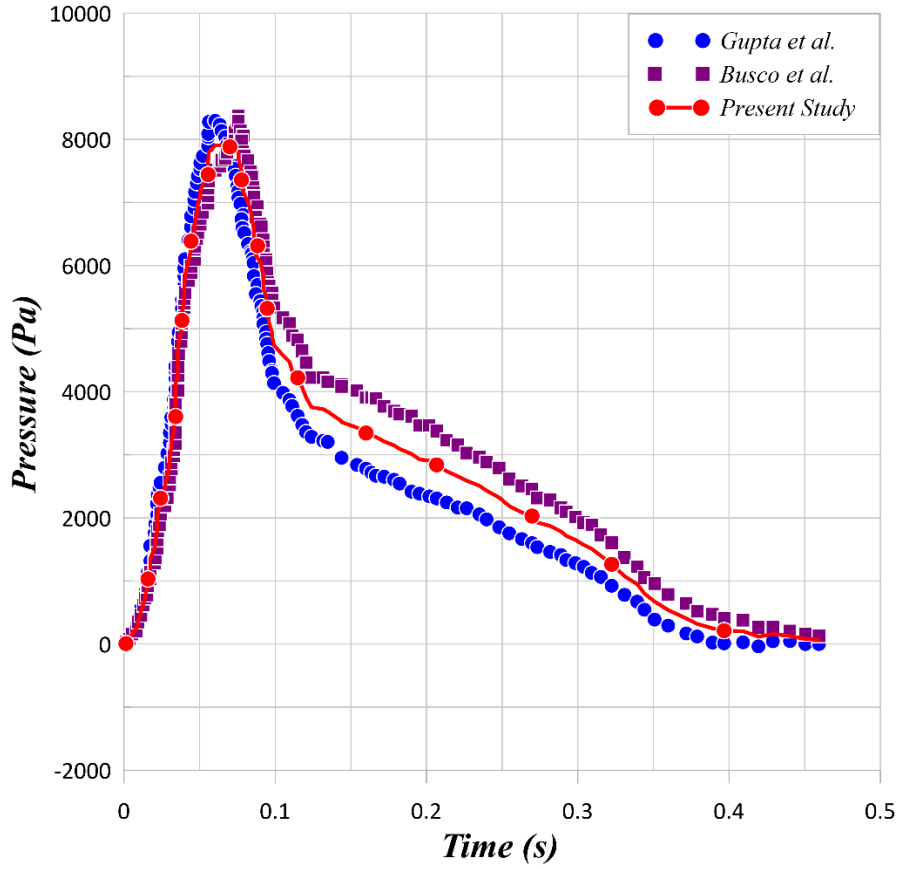


$t = 15.0s, T = 20^\circ C,$   
 $(20\mu m < d_p < 100\mu m, N_{particle} \sim 3,455K), (100\mu m < d_p < 300\mu m, N_{particle} \sim 842K)$   
 $(300\mu m < d_p < 500\mu m, N_{particle} = 480K), (500\mu m < d_p < 1000\mu m, N_{particle} = 223K)$

540  
541  
542  
543  
544  
545

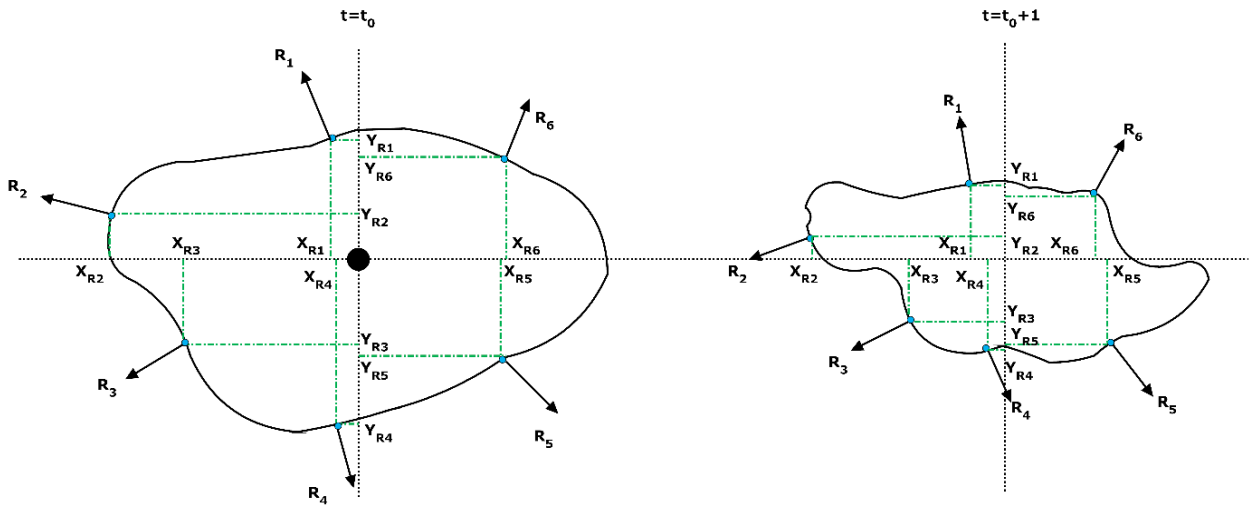


546 Fig.1 The schematic view of a) the investigated bus and sneezing person, b) seat position and key dimensions.  
547  
548



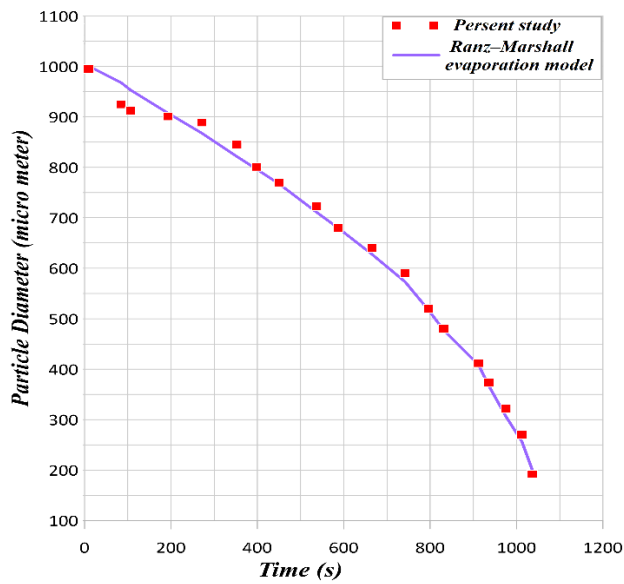
549  
550  
551  
552

Fig.2 Two models of sneezing pressure profile based on Gupta [40] and Busco [12] for 20~50 years old person and the average of this model as pressure profile ( $T_{in}=25^{\circ}C$ ,  $25\text{ m/s} < \text{Velocity} < 150\text{ m/s}$ ).

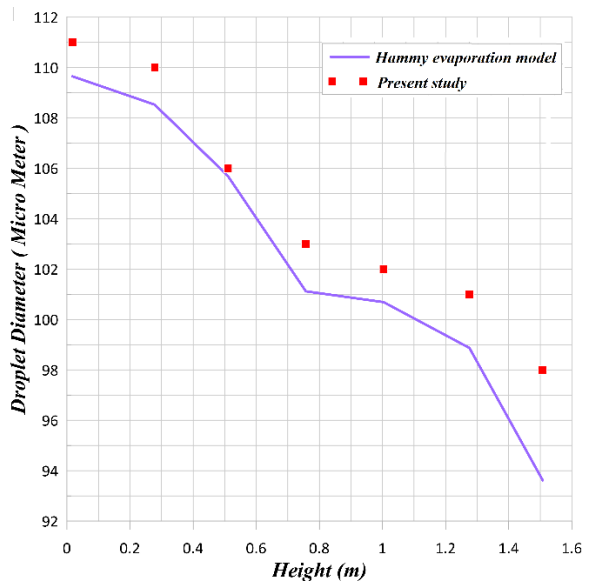


553  
554  
555  
556

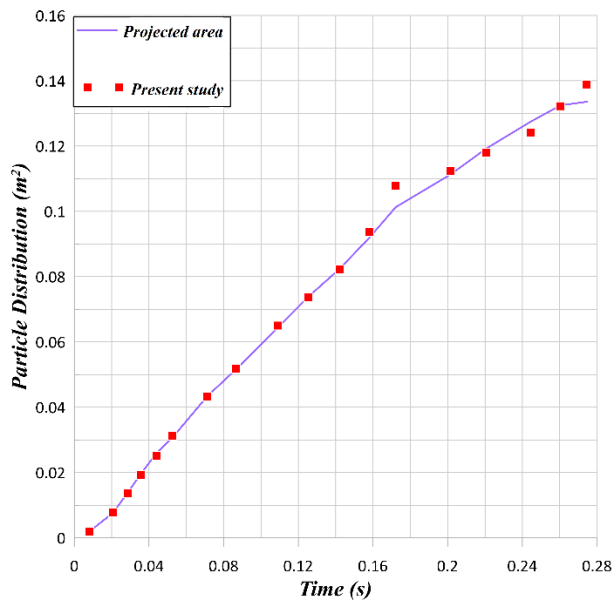
Fig.3. Calculation method for the surface and volume of the droplet by NODE algorithm.



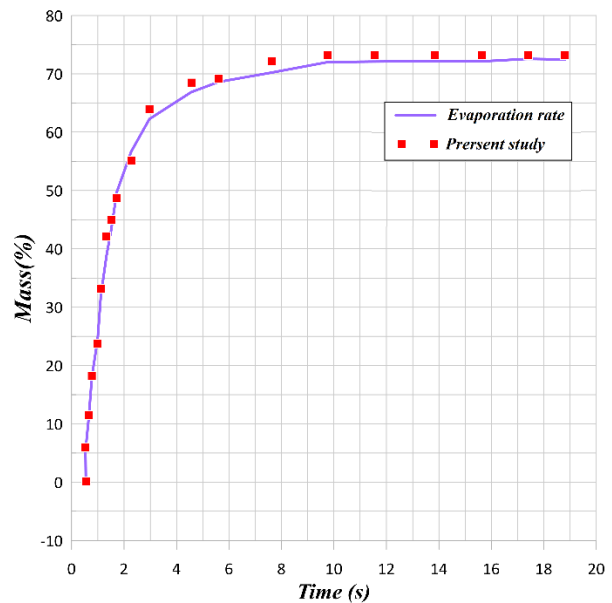
(a)



(b)



(c)

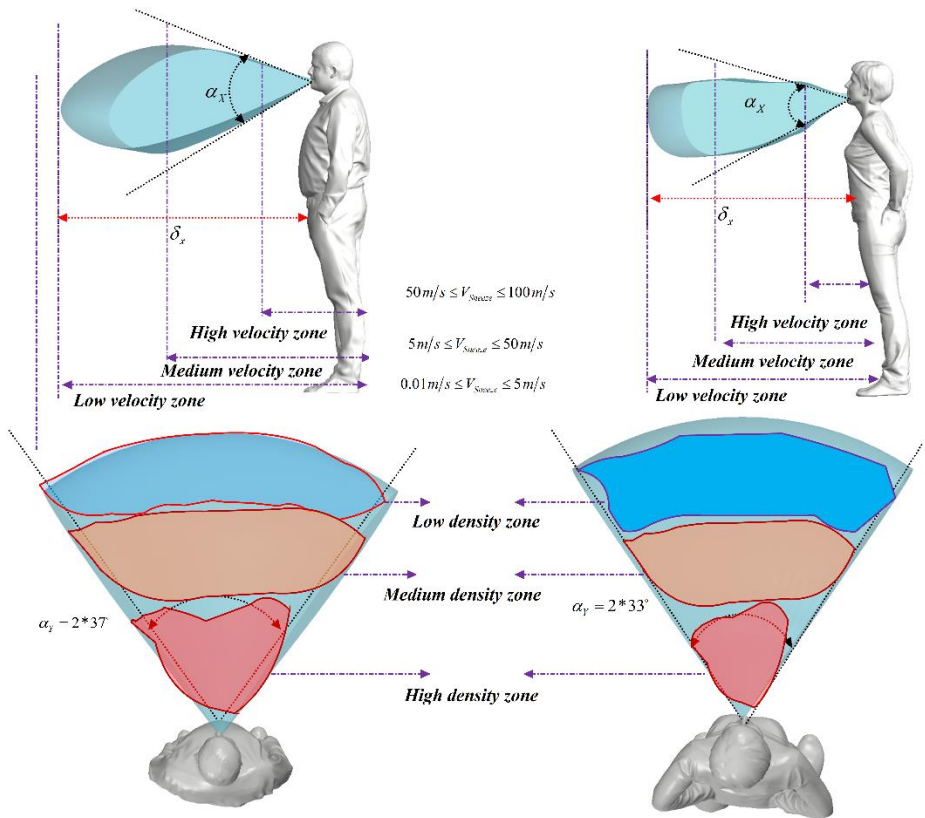


(d)

557 Fig 4. Validation for numerical method base on a) Ranz- marshal equation [41], b) Hamey evaporation model [42], c)  
 558 Busco particle distribution [12], d) mass profile [12].

559

560

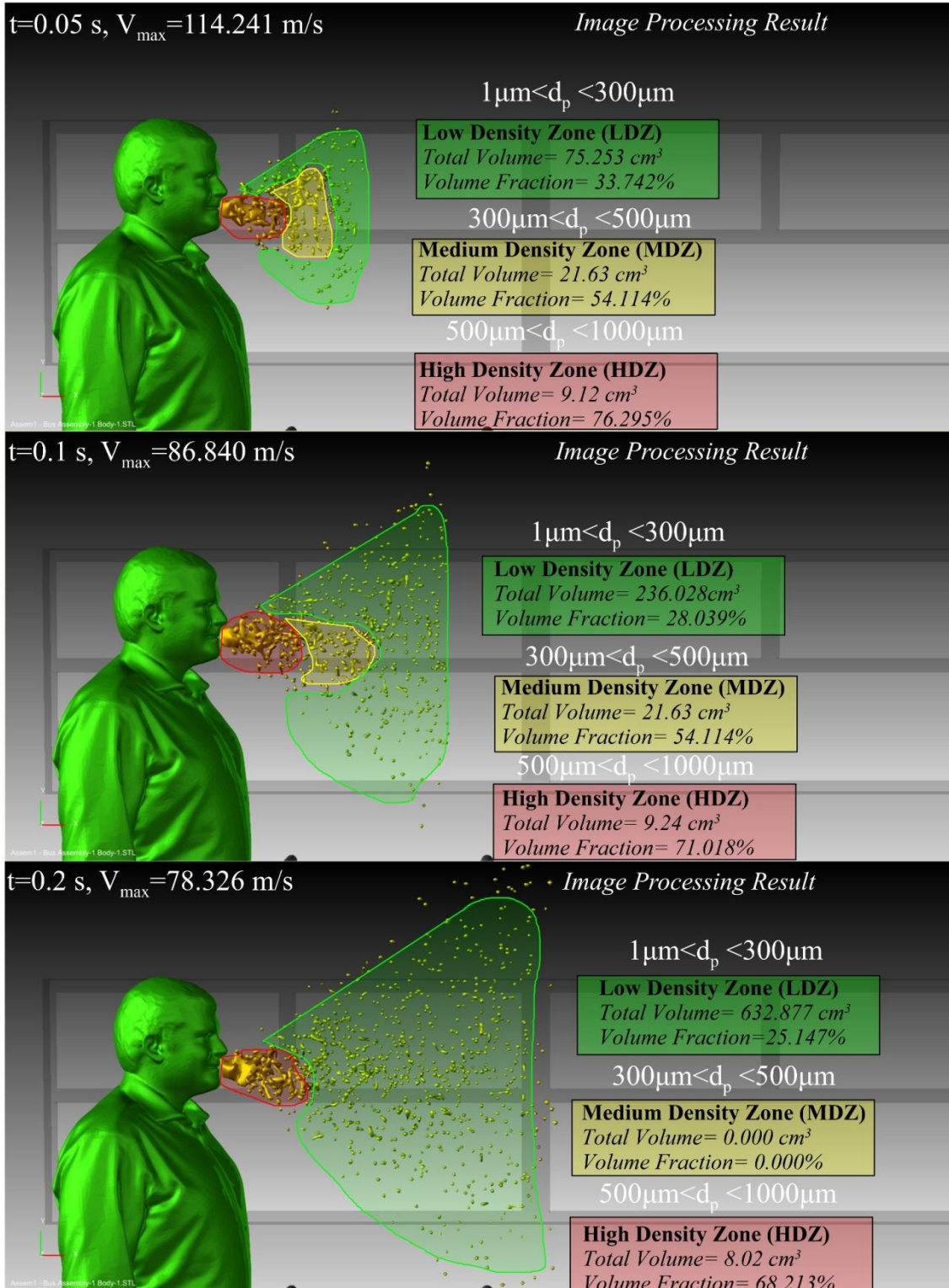


561

562

563

Fig.5. The distribution of droplets and angle of separation for different genders, based on the image processing method.

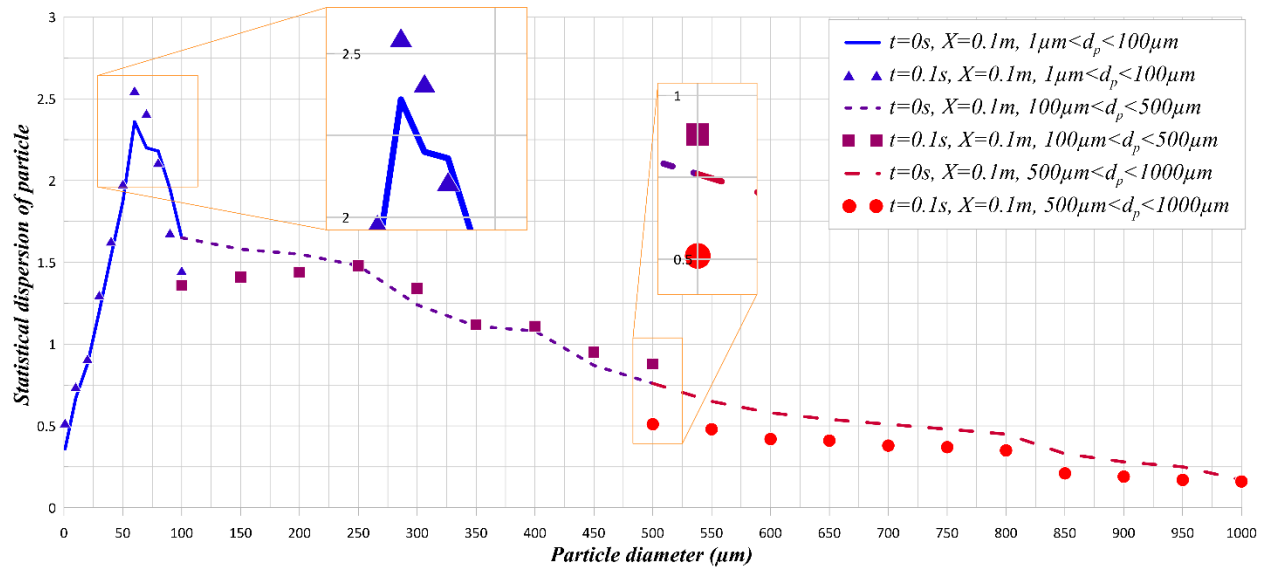


564  
565  
566  
567

Fig.6. Distribution and breakup of the saliva droplets in the vicinity of the sneezing person ( $T_{inf}=25^{\circ}C$ , Velocity=90 m/s, number of droplets=5,000,000, t=0.1s).

568

569



570

571

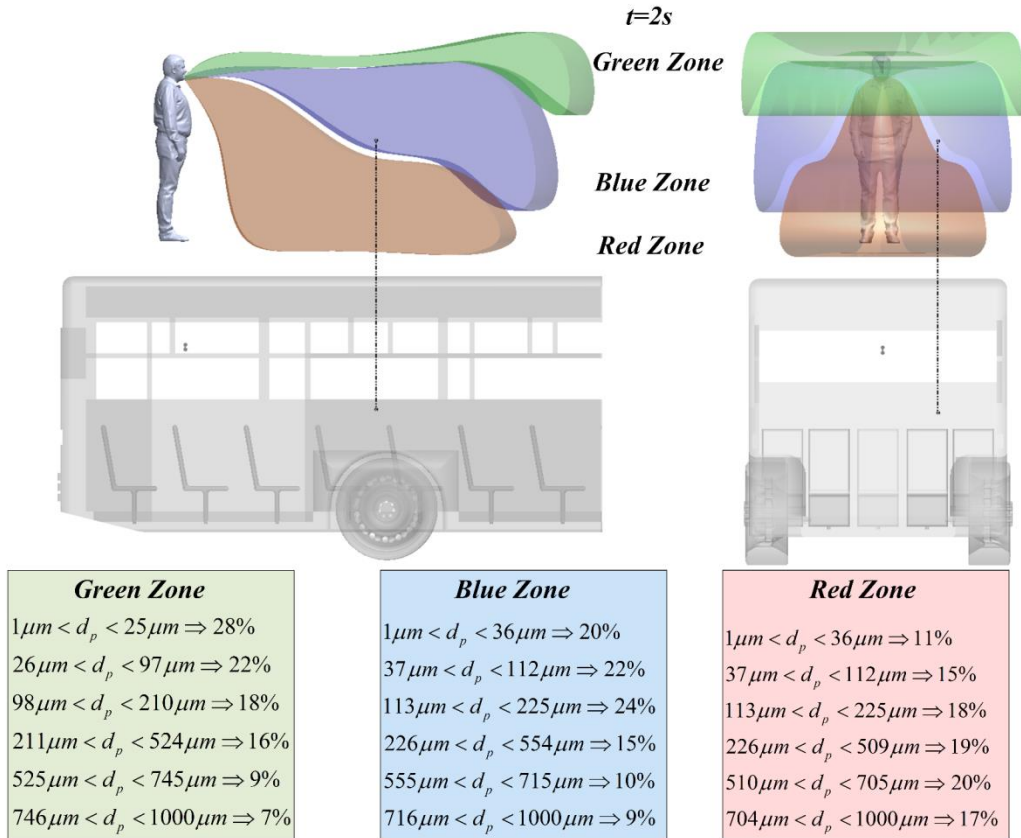
572

573

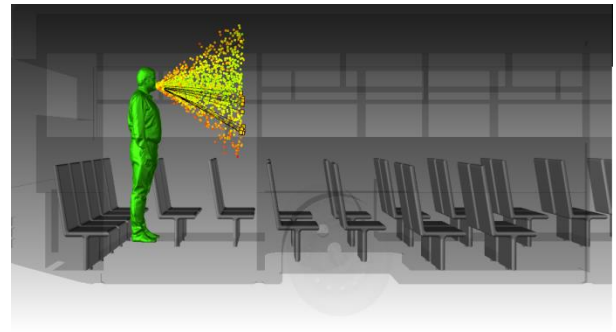
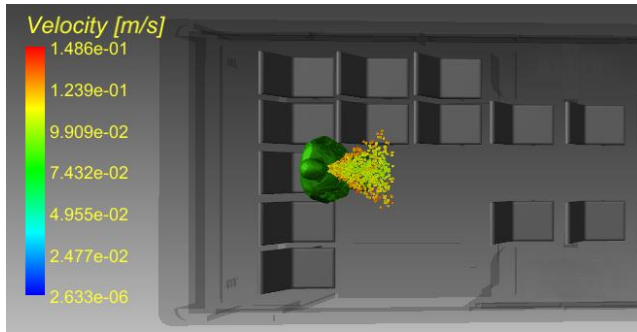
574

575

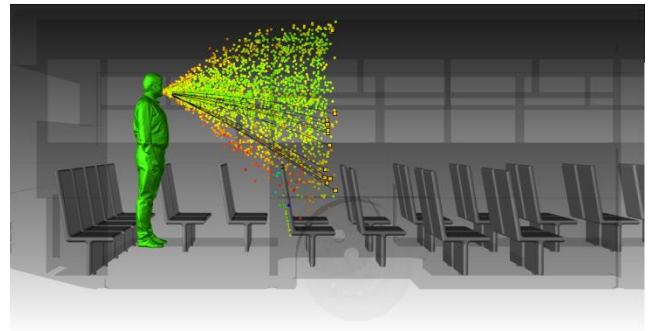
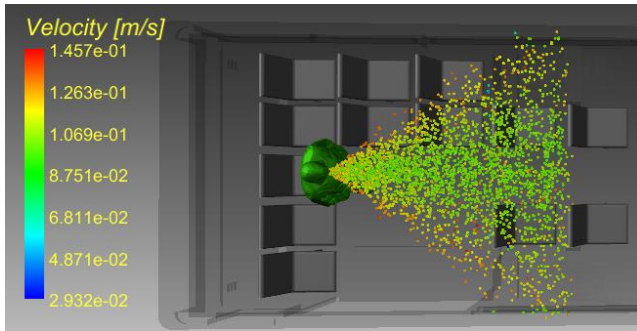
Fig.7. Frequency of droplet diameter at X=2m and for T<sub>inf</sub>=25°C.



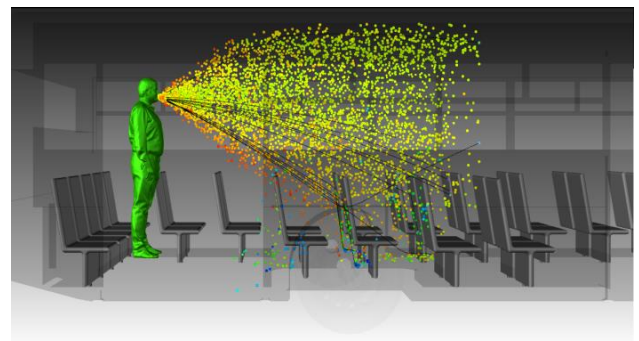
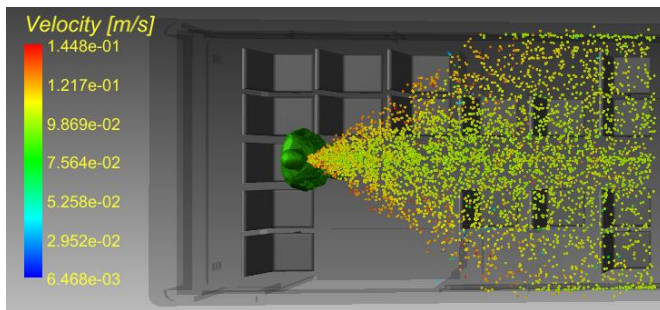
(a)



t=0.1s



t=0.5s

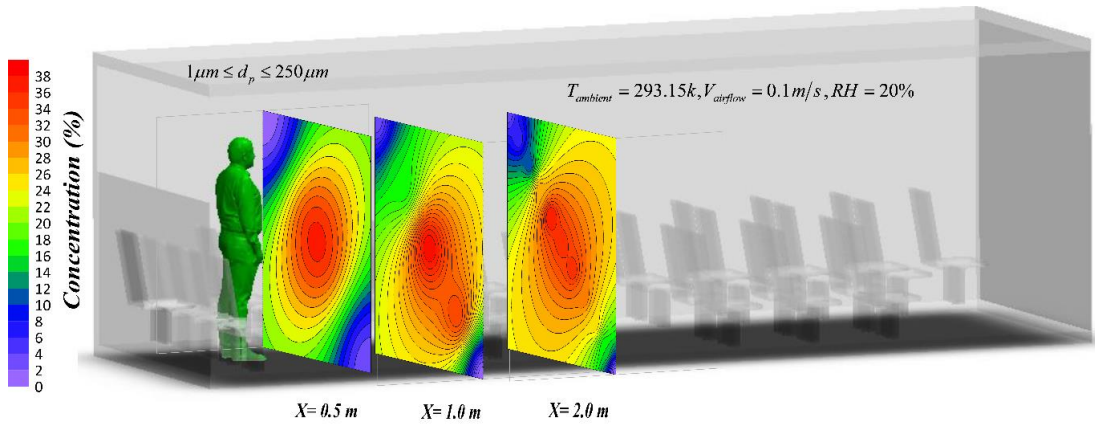


t=2s

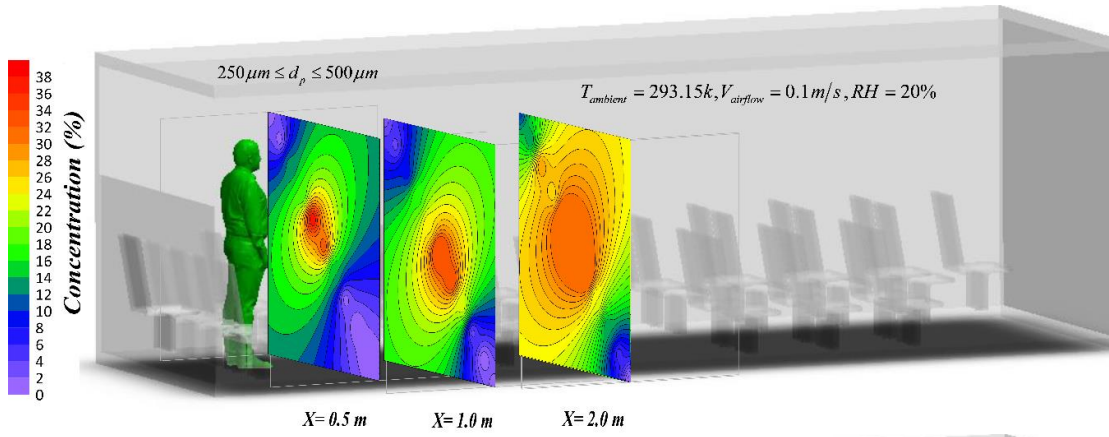
(b)

576 Fig. 8. Image processing detection of the distribution of selected droplets at t=0.1s, t=0.5s and t=2s a) side view b) top  
 577 view ( $T_{inf}=25^{\circ}\text{C}$ ).  
 578  
 579

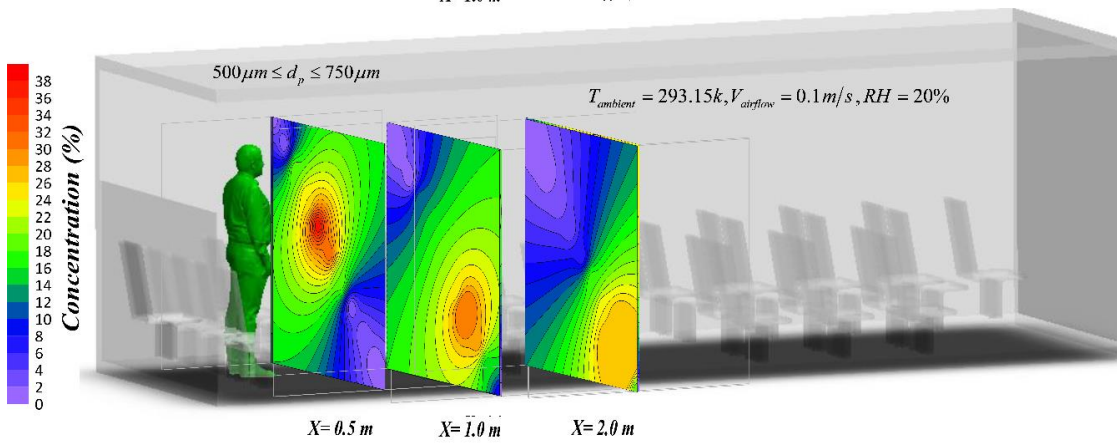
(a)



(b)



(c)



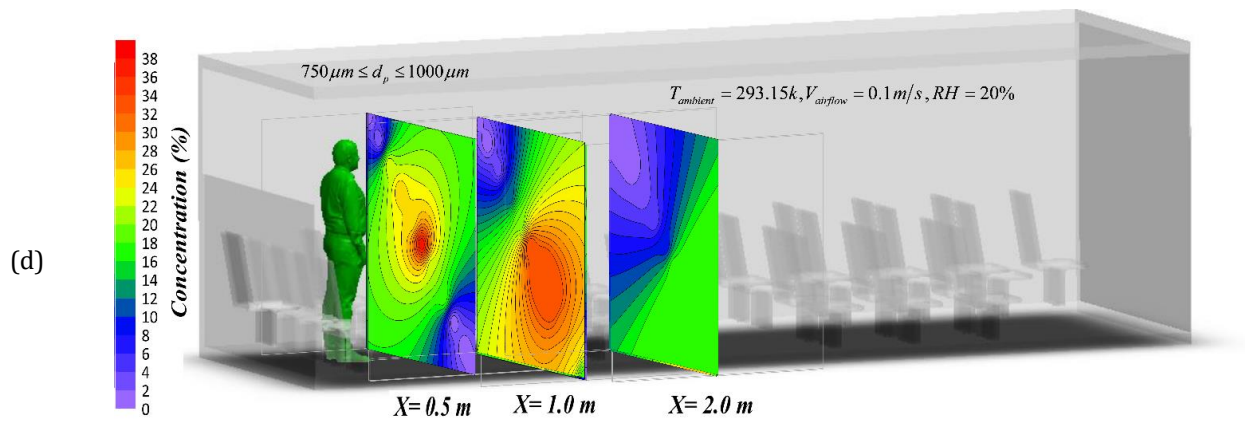
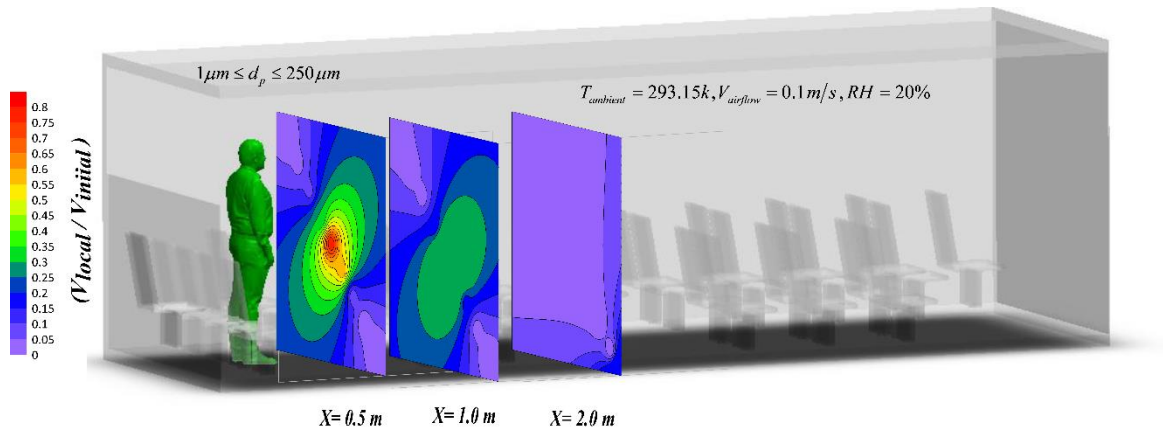


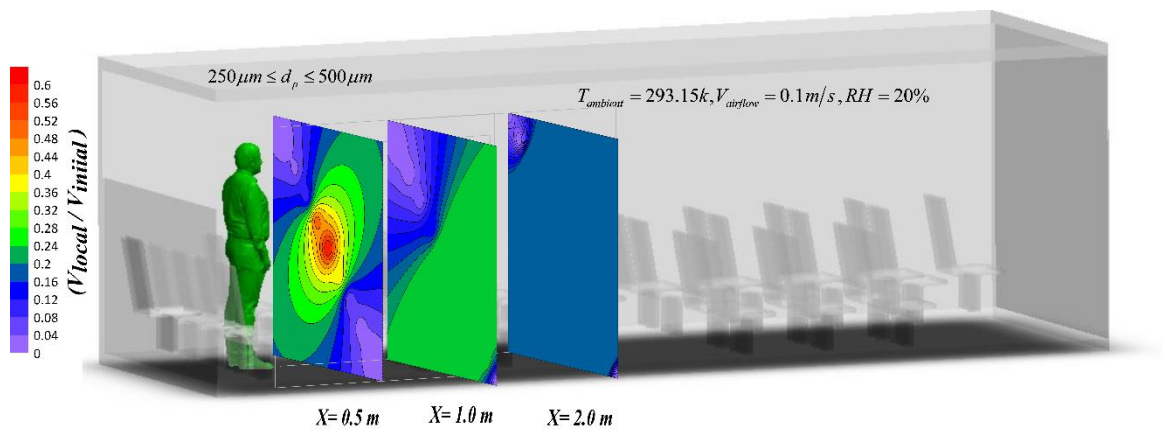
Fig. 9. Spatial distribution of the droplet concentration in 2m distance from the sneezing person for a) 1-250 micron, b) 250-500 micron, c) 500-750 micron, d) 750-1000 micron droplet diameter at t=5s after sneezing.

580  
581  
582  
583  
584  
585  
586  
587  
588  
589  
590  
591  
592  
593  
594  
595  
596  
597

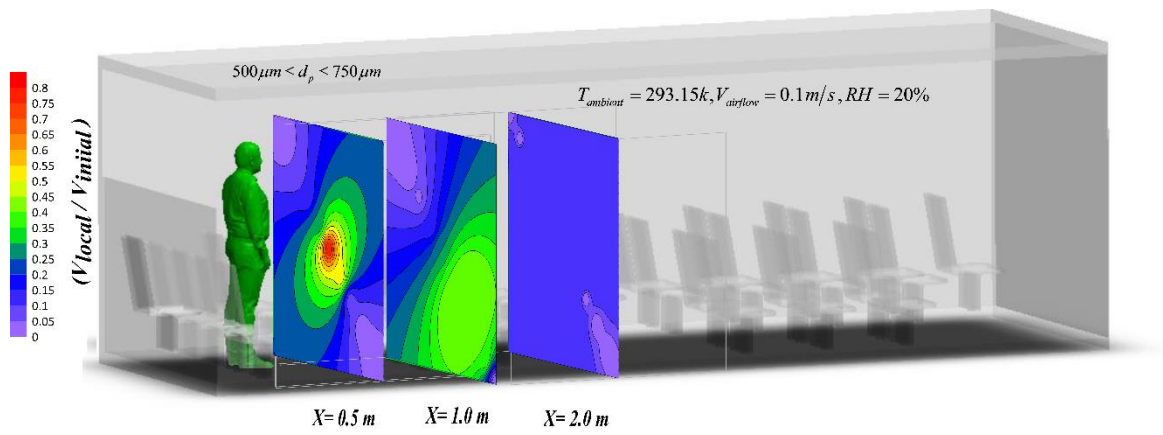
(a)



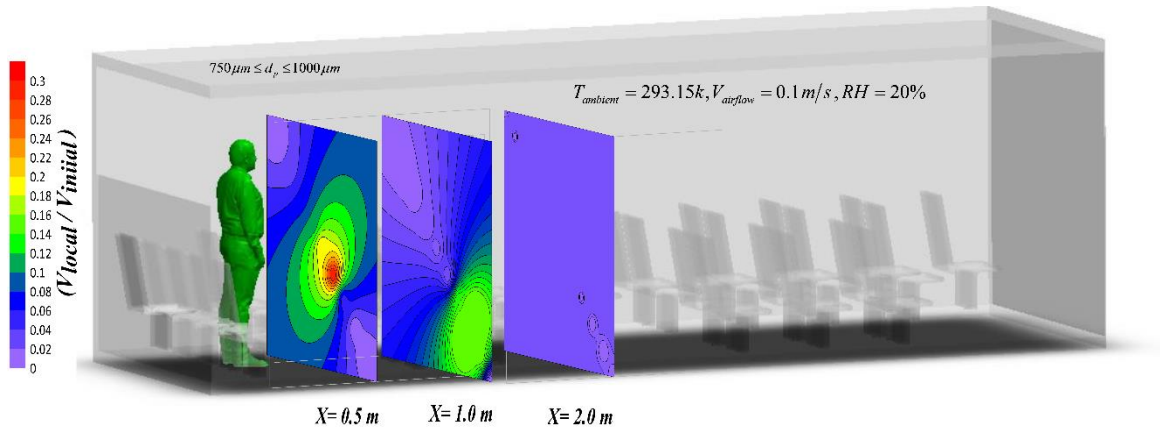
(b)



(c)



(d)



598 Fig.10. Non-dimensional velocity for the droplets distribution within 2m distance from the sneezing person for a) 1-  
599 250 micron, b) 250-500 micron, c) 500-750 micron, d) 750-1000 micron droplet diameter at  $t=5\text{s}$  after sneezing.

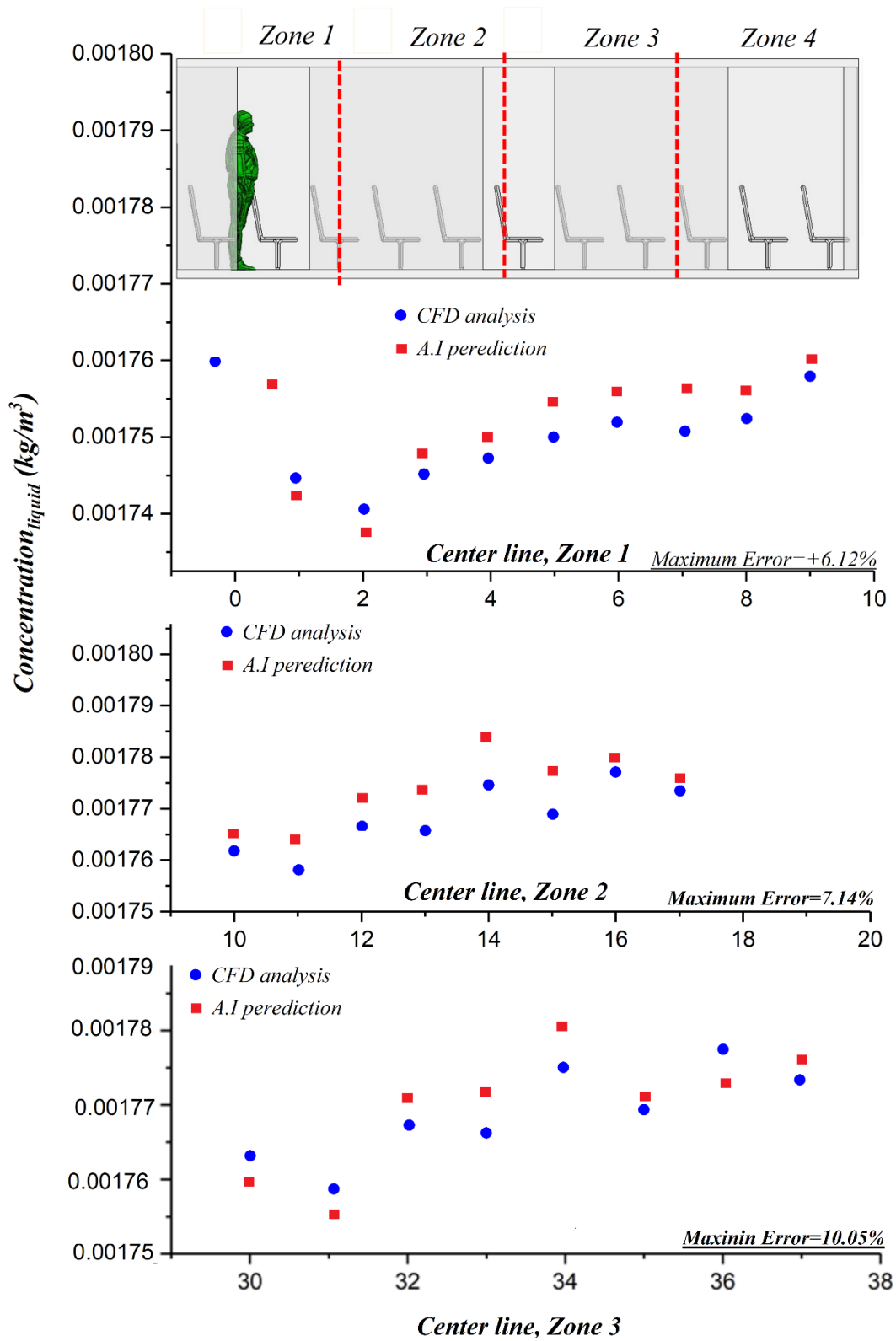
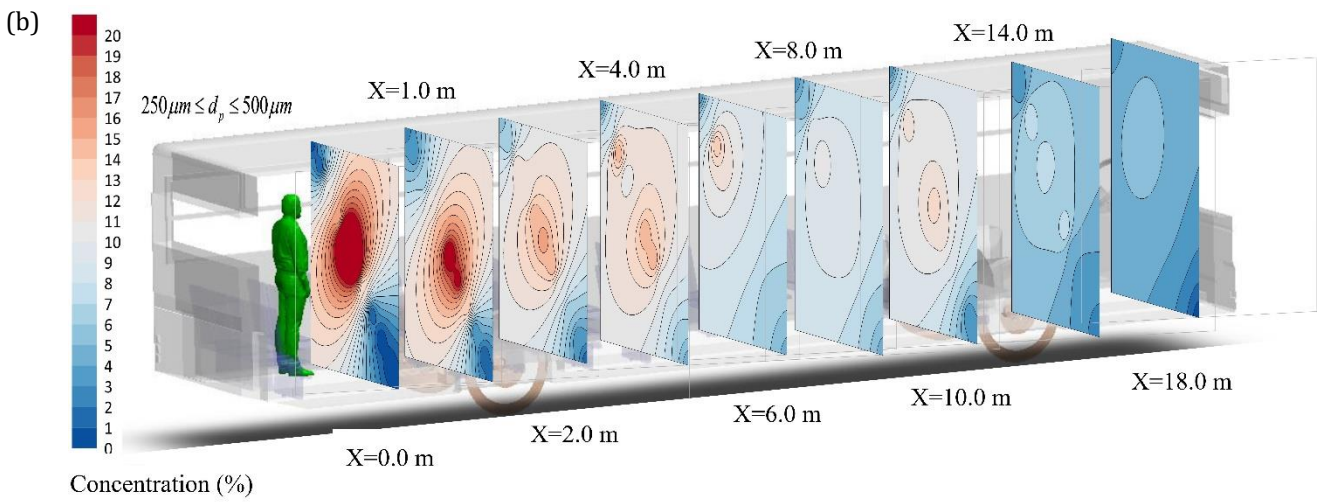
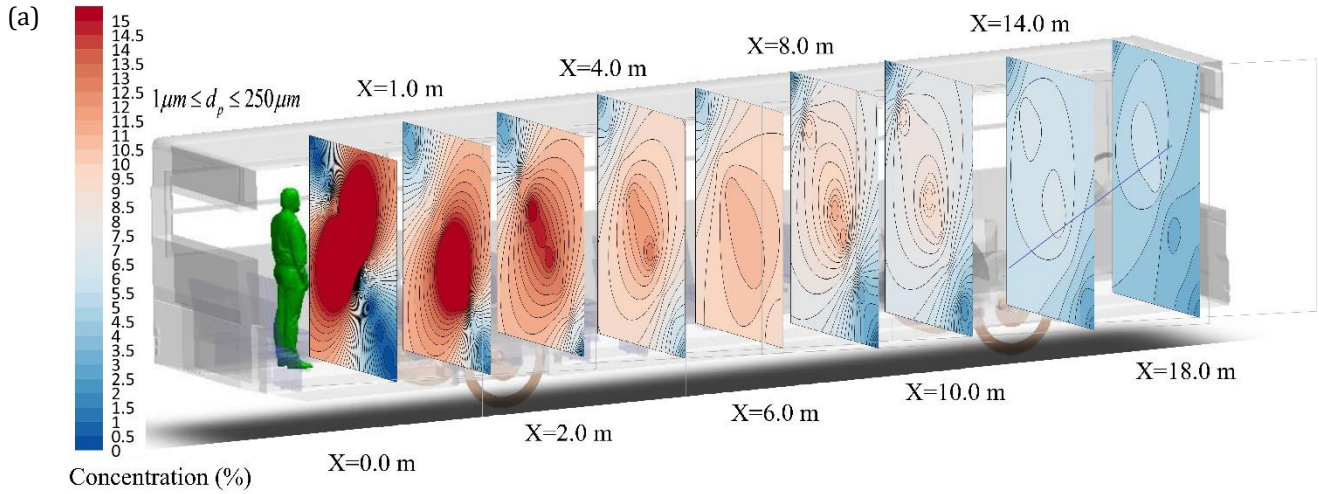
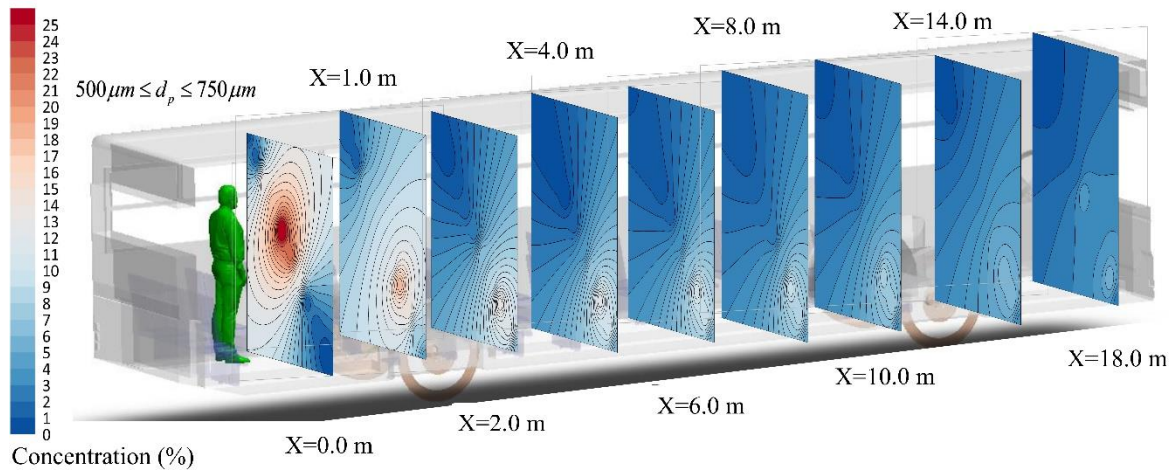


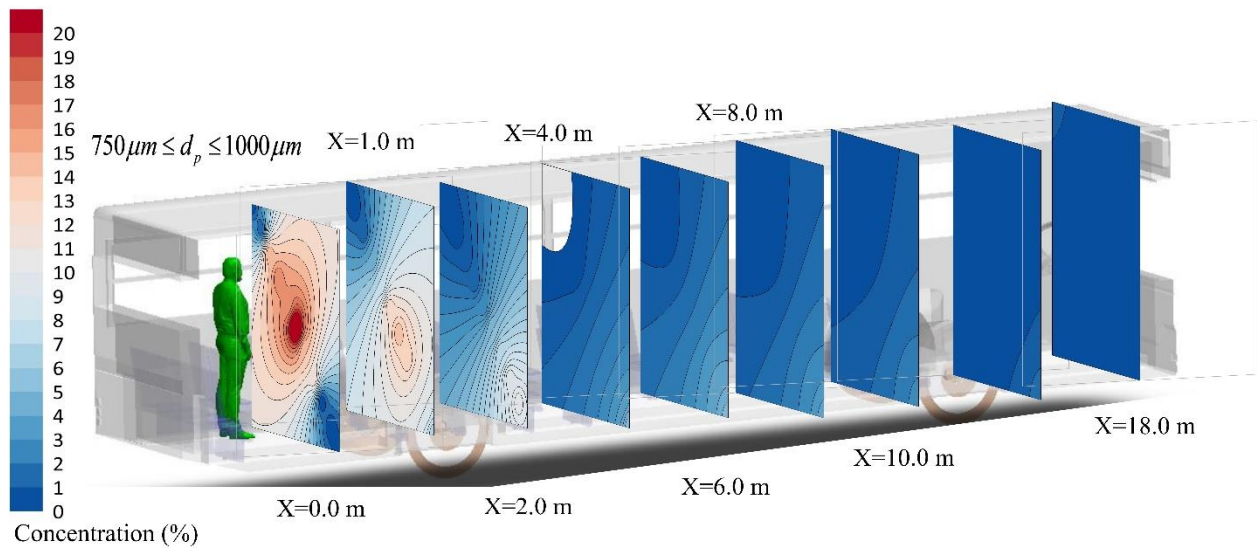
Fig. 11. Comparison between the CFD results and AI predictions at different locations along the bus.



(c)



(d)



602 Fig. 12. Distribution of the droplet concentration in 18m distance from the sneezing person for a) 1-250 micron, b)  
603 250-500 micron, c) 500-750 micron, d) 750-1000 micron droplet diameter at  $t=10\text{s}$  after sneezing.

604

605

606

607

608